



### Ambient Noise Rayleigh Wave Tomography of New Zealand

Journal:	<i>Geophysical Journal International</i>
Manuscript ID:	GJI-06-0421
Manuscript Type:	Research Paper
Date Submitted by the Author:	30-Aug-2006
Complete List of Authors:	Lin, Fan-Chi; University of Colorado at Boulder, Physics Ritzwoller, Michael; University of Colorado at Boulder, Physics Townend, John; Victoria University of Wellington, School of Geography, Environment, and Earth Sciences Bannister, Stephen; GNS Science Savage, Martha; Victoria University of Wellington, School of Geography, Environment, and Earth Sciences
Keywords:	Surface waves, Crust, Rayleigh waves, Tomography, Seismic noise, Crustal structure

# Ambient Noise Rayleigh Wave Tomography of New Zealand

Fan-Chi Lin<sup>1</sup>, Michael H. Ritzwoller<sup>1</sup>, John Townend<sup>2</sup>, Stephen Bannister<sup>3</sup>, Martha K. Savage<sup>2</sup>

1 - Center for Imaging the Earth's Interior

Department of Physics

University of Colorado at Boulder

Boulder, CO 80309-0390 USA

[linf@ciei.colorado.edu](mailto:linf@ciei.colorado.edu), (303 492 0985)

2- Institute of Geophysics

School of Geography, Environment, and Earth Sciences

Victoria University of Wellington

PO Box 600

Wellington 6040, New Zealand

3- GNS Science

PO Box 30368

Lower Hutt 6315, New Zealand

## Abstract

We present the first New Zealand-wide study of surface wave dispersion using ambient noise observed at 42 broadband stations in the national seismic network (GeoNet) and the Global Seismic Network (GSN). Year-long vertical-component time series recorded between 1 April 2005 and 31 March 2006 have been correlated with one another to yield estimated fundamental Rayleigh wave Green's functions. We filter these Green's functions to compute Rayleigh wave group dispersion curves at periods of 5–50 s, using a phase-matched filter, frequency–time analysis technique. The uncertainties of the measurements are estimated based on the temporal variation of the dispersion curves revealed by 12 overlapping three-month stacks. After selecting the highest quality dispersion curve measurements, we compute group velocity maps at 7–25 s periods. These maps, and four 1-D shear wave velocity models, exhibit clear correlations with major geological structures, including the Taranaki and Canterbury Basins, the Hikurangi accretionary prism, and previously reported basement terrane boundaries.

## 1. Introduction

Surface wave tomography has proven to be very useful in imaging the crust and uppermost mantle on both regional and global scales across much of the globe. Surface waves of different periods are sensitive to seismic shear wave speeds at different depths, with the longer period waves exhibiting sensitivity to greater depths. By measuring the dispersive character of surface waves, strong constraints can be placed on the shear wave velocity structure of the crust and upper mantle.

Observations of diffuse seismic wavefields (namely ambient noise and scattered coda waves) alleviate some of the problems affecting traditional surface wave measurements made on teleseismic earthquake recordings. Recent theoretical work has revealed that under certain circumstances the Green's function between two points can be estimated from the cross-correlated recordings made at the two locations (Weaver and Lobkis, 2001a, 2001b, 2004; Derode et al., 2003; Snieder, 2004; Wapenaar, 2004; Larose et al., 2005). These results have been substantiated using earthquake coda waves (Campillo & Paul, 2003; Paul et al., 2005) and ambient seismic noise for surface waves (Shapiro & Campillo, 2004; Sabra et al., 2005a) and local body waves (Roux et al., 2005).

The scientific appeal of noise imaging lies in using pervasive and continuous seismic energy to map subsurface shear wave velocities over large areas (e.g., Shapiro et al.,

2005). Ambient seismic noise correlation has been applied successfully to data recorded by instruments in Southern California to produce high-resolution tomographic surface-wave group velocity maps at periods of 7.5–15 s (Shapiro et al., 2005; Sabra et al., 2005b). These velocity maps exhibit striking correlations with the regional geological structure: low-speed anomalies correspond to the major sedimentary basins, and high-speed anomalies to the cores of the Sierra Nevada and other mountain ranges (Shapiro et al., 2005). Yang et al. (2006) demonstrated that similar results can be obtained at larger scales and longer periods across much of Europe. Other applications have arisen with the growth of the Transportable Array component of EarthScope being tracked across California and the Pacific Northwest (Moschetti et al., 2005), in South Korea at very short periods (Cho et al., 2006), in Tibet at long periods (Yao et al., 2006), and elsewhere. Note that while most studies to date have been conducted in continental settings, oceanic applications of ambient noise correlation at very large scales also appear to be feasible (Lin et al., 2006).

New Zealand is a prime target for ambient noise surface wave tomography. It is now spanned by a modern broadband seismological network (GeoNet, Figure 1) and is surrounded on all sides by sea. This oceanic isolation, which subjects it to some of the most sustained and energetic ocean waves on Earth (e.g., Laing et al., 2000; Gorman et al., 2003), creates very high ambient noise levels that can be exploited for ambient noise tomography. The high noise levels may provide more uniform illumination of the crust than in continental locations where ambient noise imaging has been undertaken. Furthermore, the varied tectonic environments in New Zealand provide strong lateral variations in seismic wave speeds, and the findings of numerous regional studies, referred to below, are available with which to compare to the noise analysis results.

New Zealand's tectonic architecture encompasses a variety of tectonic deformation styles, including subduction, rifting, and transpression. Such different tectonic environments are expected to yield strong lateral and vertical variations in shear wave structure that is amenable to imaging with surface waves. Yet few studies of surface waves in New Zealand have been undertaken to date. This is due in part to the historical shortage of broadband seismic stations in New Zealand (a situation largely rectified now with the advent in 2001 of the GeoNet project, <http://www.geonet.org.nz/>). More fundamentally it stems from basic limitations suffered by earthquake-based surface wave tomography. In particular, previous surface wave dispersion measurements in regions like New Zealand with relatively low levels of seismicity have been based almost exclusively on teleseismic earthquakes. It is difficult to obtain reliable short-period (<20 s) dispersion measurements



1  
2  
3  
4 from distant earthquakes due to intrinsic attenuation and scattering along ray paths, and it  
5 is these short-period waves that are most useful for constraining the structure of the crust  
6 and uppermost mantle. Moreover, surface wave sensitivity functions for teleseismic  
7 events are spatially broad, which limits the lateral resolution. For these reasons, the long  
8 history of multidisciplinary research on the structure and tectonics of New Zealand (see  
9 recent publications by Davey, 1998; Stern et al., 2000; Okaya et al., 2002; Scherwath et  
10 al., 2002; Savage et al., 2004; Baldock and Stern, 2005; Reyners et al., 2006; Stern, 2006)  
11 has involved little systematic investigation of seismic surface waves. The most detailed  
12 work in New Zealand to date on surface wave dispersion was undertaken by Brisbane  
13 and colleagues (Brisbane and Stuart, 1998; Brisbane et al., 1999), who investigated  
14 the shear-wave velocity of the eastern North Island based on fundamental Rayleigh wave  
15 phase velocities at 17–73 s using teleseismic observations of four earthquakes. Surface  
16 wave observations and receiver functions have also been used recently to study the shear  
17 wave structure of the northernmost North Island (Horspool et al., 2006).

18  
19  
20  
21  
22  
23  
24  
25  
26 In this paper we apply ambient noise tomography between 7 s and 25 s period to 42  
27 broadband seismic stations distributed almost evenly across the North and South Islands  
28 of New Zealand (Figure 1), using methods reviewed by Bensen et al. (2006) and outlined  
29 in Section 2. One of the principal benefits of ambient noise tomography over traditional  
30 earthquake tomography is the ability to estimate measurement uncertainties based on the  
31 repeatability of the measurements. The error analysis and its use in identifying reliable  
32 measurements are described in Section 3. The results of group speed tomography  
33 between periods of 8 s and 23 s are presented in Section 4 and discussed in Section 5 in  
34 terms of New Zealand's regional geology. We close Section 5 with a brief illustration of  
35 the apparent azimuthal distribution of the ambient noise sources that underpin the noise  
36 correlation method.

## 2. Data processing and group velocity measurements

37  
38  
39  
40  
41  
42  
43  
44  
45  
46  
47 We have analysed continuous vertical-component seismic data spanning the period from  
48 1 April 2005 to 31 March 2006 taken from 42 stations in the GeoNet national network  
49 and the Global Seismic Network (GSN; Figure 1). The exclusive use of  
50 vertical-component data limits the subsequent analysis to Rayleigh waves. Bensen et al.  
51 (2006) discuss at length the data processing scheme that precedes ambient noise  
52 tomography and we make only minor modifications here.

53  
54  
55  
56  
57  
58  
59  
60  
The data are processed one day at a time in single-station and station-pair steps. First,

1  
2  
3  
4 single station processing begins by removing the daily trend, mean, and instrument  
5 response from each record to create raw velocity seismograms. Next, unwanted events  
6 such as earthquake signals and instrumental irregularities (spikes) are removed by what  
7 Bensen et al. (2006) refer to as temporal normalization. Earthquakes occur regularly  
8 throughout much of New Zealand and north of the country along the Tonga-Kermadec  
9 trench, in particular, and cross-correlations of raw data tend to be contaminated by any  
10 earthquakes represented in the data. We undertake temporal normalisation to ameliorate  
11 the otherwise contaminating effects of earthquakes on the noise correlations. During this  
12 step, the raw velocity seismograms are first bandpass filtered to 15–50 s periods. This  
13 band contains the most energetic surface waves arriving after earthquakes. Then the  
14 absolute value of this signal is smoothed with a 128 s-duration moving window to  
15 provide the envelope function. The 5–100 s period bandpass-filtered raw velocity  
16 seismograms are then weighted by the inverse of the envelope function to complete the  
17 temporal normalization process. Bensen et al. (2006) provide further details of how  
18 tuning the temporal normalization to regional earthquake characteristics helps diminish  
19 unwanted correlations further.

20  
21  
22  
23  
24  
25  
26  
27  
28  
29 The temporally normalized signals are next whitened in the frequency domain. This  
30 completes the single-station preparation, after which the day-long waveform at each  
31 station is correlated with that of each of the other stations and the daily results added  
32 together to produce one 12-month stack and 12 three-month stacks. The three-month  
33 stacks are used to estimate the uncertainty in each dispersion measurement, as discussed  
34 further in the Section 3.

35  
36  
37  
38  
39  
40  
41  
42  
43  
44  
45  
46  
47  
48  
49  
50  
51  
52  
53  
54  
55  
56  
57  
58  
59  
60  
Figure 2 shows an example of 12-month stacks of broadband (5–100 s) cross-correlations  
plotted as a record-section with respect to station BFZ (Birch Farm). Clear signals are  
seen for both positive and negative correlation lags with physically reasonable move-outs  
(2–3 km s<sup>-1</sup>). The signals at positive and negative lags represent paths travelling in  
opposite directions: they sample the same media, and are expected to exhibit the same  
velocities and dispersion characteristics. For this reason, we average the positive- and  
negative-lag signals to form what we refer to below as the “symmetric-component”.

Figure 3 displays 12-month symmetric-component cross-correlations between stations  
DSZ (Denniston North) and HIZ (Hauti) for different period bands. The earlier arrivals  
at longer periods result from normal dispersion of the signals in which longer periods  
travel faster than shorter periods. Figure 4a compares a broadband cross-correlation with  
its symmetric-component for stations EAZ (Earnsclough) and THZ (Top House).

As in earthquake dispersion analysis (e.g., Ritzwoller and Levshin, 1998), the dispersion

1  
2  
3  
4 measurement applied to ambient noise cross-correlations is based on Frequency–Time  
5 Analysis (FTAN) in a two-step process applied to each pair of stations. However, the  
6 procedure applied here is automated, whereas the earthquake analysis typically involves  
7 manual intervention by an analyst. Bensen et al. (2006) discuss the dispersion  
8 measurement procedures used in this paper in greater detail, and here we provide only a  
9 brief summary. The first phase of traditional FTAN involves the construction of a  
10 two-dimensional diagram of signal power as a function of time or group velocity and the  
11 central frequency or period of successive narrow-band Gaussian filters (Figure 4c). The  
12 automatic procedure used here tracks the local power maximum along the period axis.  
13 The group arrival times of the maximum amplitude as a function of filter period are used  
14 to calculate a preliminary (raw) group velocity curve. Formal criteria are used to identify  
15 and reject curves with distinctly irregular behaviour or to interpolate through small  
16 spectral holes by selecting realistic local rather than absolute maxima. The second part of  
17 the FTAN method is the application of a phase-matched or anti-dispersion filter (Figure  
18 4d). In the non-automated method that has been applied to large numbers of earthquake  
19 records previously, the analyst defines both the phase-matched filter and the frequency  
20 band of the measurement. In the automated method employed here, the frequency band of  
21 interest is pre-set and the phase-matched filter is defined by the dispersion curve  
22 identified in the first step of the analysis. In both the manual and automated analyses, the  
23 actual frequency of a given filter is found from the time derivative of the phase at  
24 selected amplitude maxima (Levshin and Ritzwoller, 2001). Bensen et al. (2006) also  
25 discuss the use of similar methods to measure phase velocities, but only group velocities  
26 are considered here.

27  
28 We depart from the method of analysis advocated by Bensen et al. (2006) in that for data  
29 from New Zealand we can increase the number of measurements by performing the  
30 FTAN and phase-matched filtering procedures in four overlapping period bands (5–14 s,  
31 10–25 s, 15–35 s, 20–50 s). This is because in spite of applying spectral whitening to the  
32 single-station data, the spectra of the correlation signals are not completely white, but are  
33 stronger in some bands than others. Breaking the dispersion analysis into sub-bands after  
34 cross-correlation effectively flattens the amplitude spectra and improves the  
35 measurements in many cases. The dispersion curves at the edges of each period band,  
36 however, do not match perfectly and nor do the FTAN diagrams, as evidenced by the  
37 precursory artefact at about 20 s period in Figure 4d. At periods for which we have two  
38 measurements we use the group velocities with lower average uncertainty. We discuss  
39 this further in Section 3.  
40  
41  
42  
43  
44  
45  
46  
47  
48  
49  
50  
51  
52  
53  
54  
55  
56  
57  
58  
59  
60

Figure 5b shows group speed curves between stations DCZ and LTZ, OUZ and QRZ, KHZ and ODZ, and PXZ and WCZ along paths through four distinct geological regions (Figure 5a). As noted above, the curves do not meet seamlessly between the four frequency bands in which they are measured, but off-sets tend to be small. In general, a Rayleigh wave samples to a depth of approximately one-third its wavelength. Low wave speeds at short periods (<15s) usually indicate sediments near the surface and high wave speeds usually are associated with the intra-crustal roots of mountain ranges or metamorphic terranes. The lowest wave speeds at short periods in Figure 5b are for path OUZ–QRZ due to offshore sediments. On the other hand, at longer periods, waves begin to sample the upper mantle and a relatively short period onset of high group speeds is related to thin crust because the high-speed mantle is nearer to the surface. In general, both the on-set of rising and the slope of the dispersion curve from about 20–30 s provides information about both crustal thickness and upper mantle shear velocity. Note that the DCZ–LTZ path is through the Southern Alps, an area considered to have the thickest crust in New Zealand (e.g., Eberhart-Phillips and Bannister, 2002), and has the flattest group speed curves at 20–30 s periods; the significance of these features is discussed in section 5.

### 3. Error analysis and data selection

The automated measurement procedure must be accompanied by the application of criteria that identify the most reliable measurements. There are four such criteria: (1) a period cut-off related to inter-station distance, (2) signal-to-noise ratio (SNR), (3) repeatability of the measurements (particularly seasonal variability), and (4) coherence across the set of measurements. The formal uncertainty analysis is based on seasonal variability.

First, for closely spaced station-pairs, the signals at positive and negative lags can interfere with each other at long periods, rendering the measurements unreliable. This effect can be mitigated by introducing a period cut-off in which measurements are accepted only if the inter-station distance is greater than  $\sim 3$  wavelengths. A typical phase speed of  $\sim 4 \text{ km s}^{-1}$  provides a rule-of-thumb under which we accept a measurement only below the cut-off period of  $\Delta/12 \text{ s}$ , where  $\Delta$  is the inter-station distance in kilometres. Experience shows that this is near the period at which measurements deteriorate, being less repeatable and more subject to changes associated with small variations in the measurement process. The KHZ–PDZ measurement in Figure 5b, for example, cuts off at a period of about 33 s.

1  
2  
3  
4  
5  
6  
7  
8  
9  
10  
11  
12  
13  
14  
15  
16  
17  
18  
19  
20  
21  
22  
23  
24  
25  
26  
27  
28  
29  
30  
31  
32  
33  
34  
35  
36  
37  
38  
39  
40  
41  
42  
43  
44  
45  
46  
47  
48  
49  
50  
51  
52  
53  
54  
55  
56  
57  
58  
59  
60

Second, the quality of the dispersion measurement is highly correlated with the signal-noise-ratio (SNR) of the cross-correlation. We compute spectral SNR by applying a series of narrow band-pass filters and measuring signal-to-noise levels after returning to the time-domain. The signal level is defined as the peak amplitude in the arrival window and the noise level as the root-mean-square (RMS) noise in the noise window, where the arrival window spans the interval from 75 s before until 75 s after the expected Rayleigh wave group times taken from the 3-D model of Shapiro and Ritzwoller (2002) at the minimum and maximum periods of the pass-band,. The noise window starts 500 s after the end of the signal window and ends at 2700 s lag time. Figure 4b shows examples of spectral SNR for the positive and negative lag signals in Figure 4a and the corresponding symmetric-component. With extreme asymmetry (for example in Figure 4b, at periods of <10 s), the symmetric-component SNR can be degraded by the lag containing the weaker signal. However, in general, the symmetric-component has a better or at least comparable SNR relative to a single lag (Figure 4b, at periods >10 s) which is why we use it to obtain the dispersion measurements rather than using one or the other of the two lags. The SNR is typically highest at the New Zealand stations below periods of about 20 s (the microseism band) and deteriorates rapidly at periods above about 25 s. This is one reason why the analysis in this paper concentrates on periods below 30 s, the other being that measurements at longer periods require inter-station spacing exceeding 360 km. Such long paths lie exclusively along the strike of New Zealand, and therefore azimuthal coverage above about 20 s period is poorer than at shorter periods for which more inter-station paths exist.

Third, we require that a measurement be repeatable in order to use it for tomography. To quantify repeatability, we measure the seasonal variability of each measurement and then equate this with measurement uncertainty. To compute seasonal variability, we use the twelve three-month stacks represented in the data (Jan06–Feb06–Mar06, Feb06–Mar06–Apr05, ..., Dec05–Jan06–Feb06; i.e., assuming annual periodicity) in our data set and the dispersion curves measured on each of them (Figure 6). At each period and for each pair of stations, we consider a measurement potentially reliable if there are more than seven three-month stacks with SNR values higher than 15. We then compute the standard-deviation (STD) of the group speeds and arrival times using the three-month stacks meeting this condition. We screen out all the station-pairs with either a group speed STD higher than  $100 \text{ m s}^{-1}$  or an arrival time STD exceeding 4 s. The results for the average group velocity STD for the four period bands we use in the dispersion measurement process are plotted in Figure 7. The uncertainties increase at the edges of

1  
2  
3  
4 each period band. As noted above, at periods spanned by more than one analysis band,  
5 the data from the band giving the smaller uncertainty is chosen. For example, at 21 s  
6 period, the 15–35 s-band measurement yields the lower average STD group velocity and  
7 is therefore chosen to provide the measurement at 21 s period.  
8  
9

10 The number of measurements that satisfy these criteria, the average SNR, the average  
11 group speed uncertainty, and the average arrival time uncertainty at each period are  
12 summarized in Figure 8. Note that above 25 s period, very few measurements meet the  
13 selection criteria, which limits tomography to periods below this threshold. Figure 9 plots  
14 all the paths satisfying these criteria at 8 s, 13 s, 18 s, and 23 s periods. At the longer  
15 periods, the propagation paths are increasingly confined to the long axes of the North and  
16 South Islands due principally to the three-wavelength inter-station spacing criterion.  
17 Paths orthogonal to the strike of the islands exist in fairly large numbers at 8 s period and  
18 also at 13 s period.  
19  
20  
21  
22  
23  
24

#### 25 **4. Group speed tomography**

26 The Rayleigh wave dispersion measurements from one-year cross-correlations are used to  
27 invert for group velocity maps at selected periods on a  $0.25^\circ \times 0.25^\circ$  grid spanning onshore  
28 New Zealand and the surrounding region, using the tomographic method of Barmin et al.  
29 (2001). This method is based on minimizing a penalty functional composed of a linear  
30 combination of data misfit, model smoothness, and the perturbation  $\mathbf{m}$  to a reference  
31 model  $\mathbf{m}_0$  for isotropic wave speed. The measurement uncertainties discussed in the  
32 previous section (STD of group velocities) are incorporated in the inversion and in  
33 regions of poor data coverage the estimated model blends smoothly into the reference  
34 model. No adequate crustal reference model exists on the scale of this experiment, so we  
35 have used the average of the measurements at each period to define  $\mathbf{m}_0$ . A more detailed  
36 discussion of this method is given by Barmin et al. (2001) and a recent application can be  
37 found in Yang et al. (2006).  
38  
39  
40  
41  
42  
43  
44  
45  
46

47 Damping parameters weight the relative influence of data fit, smoothing, and tendency to  
48 merge the estimated model into the background model and the choice of these parameters  
49 is somewhat subjective. We perform a series of tests using different combinations of these  
50 parameters to determine acceptable values by considering data misfit, model resolution,  
51 and model norm. Ray theory is used to compute the surface wave travel times: in recent  
52 years, surface wave studies have increasingly underpinned diffraction tomography using  
53 spatially extended finite-frequency sensitivity kernels based on the Born/Rytov  
54  
55  
56  
57  
58  
59  
60



1  
2  
3  
4 approximation (e.g. Spetzler et al., 2002; Ritzwoller et al., 2002; Yoshizawa & Kennett,  
5 2002, Zhou et al., 2004; many others). Ritzwoller et al. (2002) showed that diffraction  
6 tomography recovers similar structure to ray theory at periods shorter than 50 s in most  
7 continental regions. In the context of regional tomography with dense path coverage,  
8 however, Sieminski et al. (2004) showed that nearly identical resolution can be achieved  
9 using ray theory as when using finite-frequency theory. In this study, we concentrate on  
10 short periods and on a region in which station coverage and the resulting ray paths are  
11 dense, so that ray theory suffices for the surface wave tomography. Dahlen and Zhou  
12 (2006) caution that group delay tomography for group speeds suffers from a simultaneous  
13 sensitivity to phase speeds, but this poses a potential problem only at much longer  
14 periods than considered here.

15  
16 Resolution is estimated using the method described by Barmin et al. (2001) with  
17 modifications presented by Levshin et al. (2005). Each row of the resolution matrix is a  
18 resolution surface (or kernel), which is a map defining the resolution at one spatial node.  
19 We summarize the information in the resolution surface by a single scalar quantity at  
20 each node, called the spatial resolution. Because the shape of the resolution surface for  
21 most nodes resembles a 2-D spatial Gaussian function, we approximate the resolution  
22 surface at each node with the best-fitting 2-D symmetric spatial Gaussian function and  
23 represent the corresponding local spatial resolution with this Gaussian function's standard  
24 deviation,  $\gamma$ . The resulting resolutions estimated across the region of study at periods of 8  
25 s, 13 s, 18 s, and 23 s are shown in Figure 10: we observe the resolution to be fairly  
26 constant at 8–18 s periods, with the average of 35 km equating to approximately half the  
27 inter-station spacing as expected for good data coverage. As expected, however,  
28 resolution deteriorates towards the coast of both main islands and because few  
29 measurement paths span the two islands at 8 s period, resolution in the vicinity of the  
30 Wanganui Basin and Cook Strait at 8 s is worse than at longer periods. At the longest  
31 period imaged here, 23 s, horizontal resolution is uniformly poor (>45 km) relative to that  
32 at shorter periods because the total number of measurements is smaller and because, in  
33 particular, very few sufficiently long paths are oriented orthogonal to the country's  
34 predominant strike.

35  
36 The tomographic results at 8 s, 13 s, 18 s, and 23 s periods are shown in Figure 11.  
37 Rayleigh wave speeds in the South Island are typically faster than in the North Island. At  
38 13 s period, the fastest speeds can be seen in the western South Island and wave speeds  
39 typically exhibit greater lateral variability in the North Island than the South Island. The  
40 lowest wave speeds are found offshore, west and east of the North Island: the western  
41  
42  
43  
44  
45  
46  
47  
48  
49  
50  
51  
52  
53  
54  
55  
56  
57  
58  
59  
60

1  
2  
3  
4 area corresponds to the Taranaki Basin, a major depocentre [King et al, 1996]. The  
5 eastern region includes the accretionary wedge in the Hikurangi subduction zone. The  
6 poorer resolution at 23 s period results in smoother tomographic features. Further  
7 discussion of the geological correlation of these features is given in Section 5.  
8  
9

10 The fits that the group speed maps provide to the data are shown in Figure 12. These  
11 histograms show the misfit for all data meeting the first three selection criteria discussed  
12 in Section 3. The final step in the data selection process (Step 4 in Section 3) is intended  
13 to ensure that we use only those measurements that agree with the data set as whole. This  
14 involves iteratively rejecting badly fitting measurements. Measurements with misfit  
15 larger than 7 s, therefore, are removed prior to obtaining the final maps shown in Figure  
16 11. The first three steps in the data selection account for the removal of nearly all the  
17 poor-quality measurements, and this final step removes only a few measurements and has  
18 only a minimal effect on the ultimate maps.  
19  
20  
21  
22  
23  
24

## 25 **5. Discussion**

### 26 **5.1. *Geological interpretation of the group velocity maps***

27  
28  
29 Many of the prominent features in the group velocity maps (Figure 11) can be clearly  
30 associated with known geological structures. In doing this, it is important to take the  
31 group velocity maps' horizontal resolution and interstation path coverage into  
32 consideration, as well as the vertical smoothing inherent in surface wave propagation.  
33 The spatial smoothing used in constructing the tomographic images results in some  
34 instances of apparent velocity variations extending offshore (such as east of the North  
35 Island and west of the South Island, in the 18 s map), and care must be taken to avoid  
36 over-interpreting this leakage.  
37  
38  
39  
40  
41  
42  
43

#### 44 **8 s group velocities**

45  
46 Low group velocities ( $<2.4 \text{ km s}^{-1}$ ) are observed west of North Island, likely reflecting  
47 thick sedimentary deposits in the greater Taranaki Basin (TB, Figure 13) offshore and to  
48 the west of Taranaki and Northland (Wood and Woodward, 2002). The velocities change  
49 sharply across the west coast of Northland due to a change in sedimentary thickness  
50 across the Northland Boundary Fault (NBF, Figure 13), which is located approximately  
51 50 km offshore and parallel to the coastline (Uruski et al., 2004).  
52  
53  
54  
55

56 Low velocities are also observed along the east coast of North Island, reflecting the  
57 presence of sedimentary basins up to 5 km deep in the Hikurangi subduction margin's  
58  
59  
60



1  
2  
3  
4 accretionary prism (AP, Figure 13; Beanland et al., 1998; Henrys et al, 2006). Similarly  
5 low velocities are also observed in the Bay of Plenty, offshore north of the Taupo  
6 Volcanic Zone (TVZ, Figure 13), where seismic reflection data reveal variable sediment  
7 thicknesses (Davey et al., 1995). The Taupo Volcanic Zone itself is rather poorly imaged  
8 at this period (cf. 13 s, below). Of perhaps more significance, however, is the fact that  
9 few station pairs exhibit high-SNR correlations at 8 s. This may be in part due to the  
10 noisy character of station TOZ in the Waikato region, which is addressed in section 5.3,  
11 but the failure of stations MWZ, MXZ, PUZ, and URZ to correlate well with HIZ at 8 s  
12 (Figure 9) suggests strong attenuation of high-frequency energy within the Taupo  
13 Volcanic Zone, as also noted by Mooney (1970), Salmon et al. (2003), and Stern et al.  
14 (2006). Moreover, the apparent widening offshore of the low-velocity areas here may  
15 simply represent a smearing out of the velocity structure along paths between  
16 Coromandel/Northland and East Cape.  
17  
18  
19  
20  
21  
22  
23

24 The group velocities east of the North Island can be compared with recent wide-angle  
25 reflection and body-wave tomography (Henrys et al., 2006; Reyners et al., 2006). Henrys  
26 et al. (2006) quote values for  $V_p$ ,  $V_p / V_s$  and Poisson's ratio of  $<5.5 \text{ km s}^{-1}$ ,  $>1.85$ , and  
27  $>0.29$ , respectively, yielding  $V_s <3.0 \text{ km s}^{-1}$  for the uppermost 15 km of the crust in  
28 Hawke Bay. This value is compatible with the velocity found in our analysis.  
29  
30  
31

32 The 8 s velocity map is much more homogeneous for the South Island. Velocities are  
33 predominantly  $>2.8 \text{ km s}^{-1}$  other than in eastern Canterbury, where lower group velocities  
34 ( $<2.4 \text{ km s}^{-1}$ ) closely correspond to the position of the Canterbury Basin (CB, Figure 13).  
35 A small region of low velocity is also observed in the northwest South Island (GID,  
36 Figure 13), east of Westport. While the horizontal resolution and path coverage in this  
37 area are poorer than elsewhere in the inland South Island, it is intriguing that this location  
38 corresponds to sedimentary deposits in the Grey-Inangahua Depression (GID) (Anderson,  
39 1979).  
40  
41  
42  
43  
44

### 45 **13 s group velocities**

46 The key features of the 13 s group velocity map are broadly similar to those at 8 s. Once  
47 again, low surface wave velocities are imaged west of Northland and Taranaki. Onshore,  
48 velocities in Taranaki (TB, Figure 13) appear to increase abruptly eastwards, at a position  
49 close to the Taranaki Fault (TF, Figure 13) and near the transition between the Brook  
50 Strait and Murihiku basement terranes (Mortimer et al., 1997). Sherburn et al. (2006)  
51 identified a sharp east–west change in mid-crustal  $V_p$  values in the same location using a  
52 3-D tomographic inversion of local earthquake travel times.  
53  
54  
55  
56  
57  
58  
59  
60

1  
2  
3  
4 A band of higher group velocities ( $>2.9 \text{ km s}^{-1}$ ) is observed west of Wellington and  
5 appears to extend all the way from Cook Strait to Lake Taupo. The location of this band  
6 closely matches the interpreted extent of Haast schist in the southern North Island  
7 (Mortimer et al., 1997; Mortimer, 2004). Schist outcrops at the surface in several  
8 locations, and is inferred to extend northwards from Cook Strait (starting at the offshore  
9 extension of the Wairau Fault), beneath the Wanganui Basin, to the Kaimanawa Ranges  
10 near Lake Taupo (Mortimer et al., 1997; Mortimer 1993). Laboratory velocity  
11 measurements on Haast schist by Godfrey et al. (2002) revealed substantial P-wave  
12 velocity anisotropy and mean (isotropic) S-wave velocities of  $3.5\text{--}3.6 \text{ km s}^{-1}$ .  
13  
14  
15  
16  
17

18 In contrast to the low number of paths crossing the Taupo Volcanic Zone at 8 s periods,  
19 the area between Rotorua and Taupo appears to be reasonably well imaged at 13 s (Figure  
20 9). The low velocities in this region are compatible with the results of previous seismic  
21 studies in this region (e.g., Stratford & Stern 2006, Harrison & White 2004) which  
22 indicate low P-wave velocities ( $< 4 \text{ km/s}$ ) in the top 2–5 km. The ash and volcanoclastic  
23 sediments present in this area not only have intrinsically low seismic velocities, but are  
24 also strongly attenuating. Such attenuation has proven an impediment to previous  
25 active-source studies of the crust in this region (e.g., Stern 1987, Stratford & Stern 2006)  
26 and has itself been a focus of several studies (Mooney, 1970; Eberhart-Phillips and  
27 McVerry, 2003; Salmon et al., 2003).  
28  
29  
30  
31  
32  
33

34 Consistently high velocities ( $>2.9 \text{ km s}^{-1}$ ) are found beneath the Southern Alps, from  
35 Fiordland as far north as the southern end of the Hope Fault. Slightly lower velocities  
36 ( $2.7\text{--}2.8 \text{ km s}^{-1}$ ) are found in Otago, and the Canterbury Basin sediments are still clearly  
37 distinguished ( $2.4\text{--}2.6 \text{ km s}^{-1}$ ). While there are few published data with which to compare  
38 these figures, we note that Godfrey et al. (2001) observed a  $\sim 5\%$  difference in P-wave  
39 velocity at 10 km depth between the southern Canterbury Basin ( $<6 \text{ km s}^{-1}$ ) and offshore  
40 Otago and Southland ( $6.0\text{--}6.6 \text{ km s}^{-1}$ ), a comparable difference to that revealed by the 13  
41 s Rayleigh wave speeds.  
42  
43  
44  
45  
46

### 47 **18 s group velocities**

48 Slow velocities ( $<2.6 \text{ km s}^{-1}$ ) are observed beneath the entire east coast of the North  
49 Island at 18 s period. Rayleigh waves of this period are likely to still be sampling the  
50 accretionary prism, but may also be influenced by the uppermost section of the subducted  
51 crust, especially along paths close to the coastline. The subducted plate is well imaged  
52 with local seismicity (Reyners et al., 2006) and deep seismic reflection data (Henrys et al.,  
53 2006): the subduction décollement dips northwest at  $3\text{--}6^\circ$  and lies at a depth of  $\sim 15 \text{ km}$   
54  
55  
56  
57  
58  
59  
60

(Henrys et al., 2006, Ansell and Bannister, 1996) beneath the coastline immediately south of Hawke Bay. Higher velocities ( $>2.8 \text{ km s}^{-1}$ ) are observed in northwest Nelson (NN, Figure 13), Fiordland, and Otago. In northwest Nelson and Fiordland these higher velocities correspond approximately to the mapped locations of the Median Batholith (Mortimer, 2004), and appear to be restricted to the northern side of the Wairau Fault. We note that high velocities are also seen in Marlborough and Cook Strait, where they are possibly associated with Haast schist.

### 23 s group velocities

Compared to the shorter-period maps, the 23 s map reveals only large features oriented along the strike of the islands. This is straightforwardly interpreted as the effect of sampling bias, because all the paths satisfying the first selection criterion in section 3 need to be longer than  $\sim 275 \text{ km}$  (Figure 9). Most of the measurements used to produce this map not only span long paths but also have a strong azimuthal bias. Thus, the 23s map only represents large-scale averages, and illustrates little local detail. The depth extent of the velocity information that results is similarly limited, as discussed further in the next section.

### 5.2. 1-D shear velocity models

Here we present four characteristic 1-D isotropic shear velocity models based on the 7–25 s tomography maps. Two points in the North Island and two points in the South Island (Figure 5a) are chosen for this purpose. For each point, the group velocities from the four adjacent grid points are taken from each tomography map, to yield the dispersion curve assigned to the central point (Figure 14a), and the spread of measurements that govern the inversion. A Monte Carlo method is then applied to obtain the 1-D shear velocity profile providing the best fit to the dispersion curve given its associated uncertainties (Figure 14b).

In the inversion, we parameterize the model to include four crustal layers and a single mantle layer. Because Rayleigh waves are more sensitive to shear velocities than compressional velocities, we fix the  $V_p/V_s$  ratio of each layer but allow its shear velocity and thickness to both vary randomly during the Monte Carlo search. In addition, because the dispersion curve between 7 s and 25 s periods only weakly constrains either the top few kilometres of the crust or the structure deeper than about 30 km, we fix the shear velocity in the uppermost crustal layer and the mantle to be  $2.55 \text{ km s}^{-1}$  and  $4.4 \text{ km s}^{-1}$ , respectively. We also impose a monotonicity constraint on the velocities in order to obtain a physically plausible model: that is, velocities must satisfy  $m_i < m_{i+t}$  where  $m_i$  is the

1  
2  
3  
4 velocity of a layer directly over a layer with velocity  $m_{i+1}$ .

5  
6 The best-fitting profiles at each of the four locations are shown in Figure 14b. Although a  
7 range of models will fit the data and a priori constraints acceptably, several aspects of the  
8 best-fitting profiles are worth mentioning. First, compared to the other regions, the  
9 Southern Alps point has the thinnest top layer, which is presumably because of the lack of  
10 sediments. In contrast, the Canterbury Basin profile has the thickest top layer which  
11 accurately reflects the thickest sedimentary deposits there relative to the other three  
12 points. Second, the Southern Alps profile is nearly homogeneous with depth. This is  
13 strikingly similar to the  $V_p$  model of Scherwath (2003) in the same region. Their model  
14 has  $V_p$  values of 5.6–6.2 km s<sup>-1</sup> between depths of 3 km and ~30 km. If we adopt a  
15  $V_p/V_s$  ratio of 1.73, the corresponding  $V_s$  values are 3.24–3.58 km s<sup>-1</sup> and compare very  
16 well with the values of 3.34–3.58 km s<sup>-1</sup> obtained in the current study (Figure 14a). Third,  
17 with group velocities only measurable to periods of approximately 25 s, crustal thickness  
18 trades off strongly with mantle velocity if the crust is thicker than about 30 km. For this  
19 reason, we can say little with confidence about crustal thickness on the basis of the noise  
20 correlation analysis performed to date, other than that the crust beneath the Southern Alps  
21 is thicker than elsewhere. The value of 35 km for the Southern Alps crustal thickness  
22 depends strongly on the mantle velocity chosen, so should not be interpreted  
23 quantitatively.

24  
25 We have also inverted the two observed dispersion curves shown in Figure 5 for the paths  
26 through the Southern Alps and the Canterbury Basin. The advantage of these inversions is  
27 that the measured curves extend to longer periods than those constructed from the  
28 dispersion maps and, therefore, constrain structures to greater depth. Inversion of the  
29 measured curves reveals similar crustal structure and thickness, but tightens the constraint  
30 on the shear velocity of uppermost mantle. The shear velocity of the uppermost mantle  
31 beneath the Southern Alps, consistent with the measured curve, is 4.19 km/s, and beneath  
32 the Canterbury Basin is 4.51 km/s. Contrast these values with 4.4 km/s, which is imposed  
33 on the inversion of the curves from the dispersion maps.

### 34 35 36 37 38 39 40 41 42 43 44 45 46 47 48 49 **5.3. Azimuthal distribution of ambient noise sources**

50 The cross-correlation results not only contain information about the speed of wave  
51 propagation between pairs of stations (i.e., the Rayleigh wave speeds at different  
52 frequencies), but also information about the azimuthal distribution of the source(s) of the  
53 ambient noise itself. A comparison of the positive and negative lags of the  
54 cross-correlation time series provides some insight into the relative strengths of the waves  
55  
56  
57  
58  
59  
60

1  
2  
3  
4 propagating in opposite directions. We present here a brief analysis of the noise  
5 directionality based on a single 12-month stack: this yearly average may mask any  
6 seasonable variability, which is the subject of ongoing research using longer records.  
7

8  
9 We separately calculate the SNR spectrum for the positive- and negative-lag components  
10 of the cross-correlation between each station-pair and multiply that by the square root of  
11 the distance between the two stations to compensate for geometrical spreading. Figure 15  
12 summarizes the results for the four periods shown in the tomographic maps of Figure 11.  
13 For each pair of stations, two arrows with opposite directions are plotted at each station.  
14 The length of the arrow is proportional to the SNR multiplied by the square root of the  
15 distance and the direction of the arrow represents the direction of wave propagation. We  
16 restrict the calculation to pairs of stations separated by a distance in kilometres larger  
17 than six times the period in seconds, rather than the 12 times used in the first selection  
18 criterion discussed in Section 3. This is because the effect of overlap between the  
19 positive- and negative-lags on the noise directivity estimates is minor compared to group  
20 velocity measurement which is sensitive to small variations.  
21  
22  
23  
24  
25  
26

27  
28 Several conclusions can be drawn from these maps. At 8 s and 13 s periods, the South  
29 Island exhibits generally stronger and more coherent signals than the North Island. The  
30 signals at 8 s predominantly arrive from the south, southwest and southeast quadrants in  
31 the South Island, whereas in the North Island they are more azimuthally uniform.  
32 Short-period energy arriving from the north appears to be minimal at South Island  
33 stations. These observations are consistent with oceanographic data, which reveal that the  
34 high-energy west, south, and east coasts of New Zealand have predominant wave heights  
35 and periods of 1–3 m and 6–8 s, ~4 m and 10–12 s, and 0.5–2 m and 7–11 s, respectively  
36 (Pickrill & Mitchell, 1979). In contrast, the low-energy north coast (between North Cape  
37 and East Cape) experiences a prevailing north-easterly swell with 0.5–1.5 m wave heights  
38 and 5–7 s wave periods.  
39  
40  
41  
42  
43  
44

45 At periods of 13, 18, and 23 s, stations TOZ, KNZ and WHZ exhibit only weak signals  
46 and are revealed by ambient noise level analysis (cf. Lin et al., 2006) to suffer from high  
47 local noise. The broadband sensor at each of these sites is a Guralp CMG-40T, which has  
48 poorer SNR characteristics than the newer Guralp CMG-3ESP and Streckheisen STS-2  
49 sensors used elsewhere (K. Gledhill, pers. comm., 2006).  
50  
51  
52

53 For periods greater than 13 s, strong waves appear to arrive preferentially from the  
54 northeast and southwest. The >150 km-long paths over which these measurements are  
55 made tend to be oriented parallel to the overall strike of New Zealand, particularly in the  
56 South Island. It is difficult, therefore, at these longer periods to infer the azimuthal  
57  
58  
59  
60

1  
2  
3 distribution of the incoming waves given highly biased sampling. For this reason, we  
4 believe that only the 8 s data adequately represent the azimuthal variability of the  
5 incoming noise.  
6  
7

## 10 6. Conclusions

11  
12 We present here the first New Zealand-wide study of surface wave dispersion using  
13 ambient noise recordings at 42 broadband stations. By correlating year-long time series  
14 between stations, we have obtained Rayleigh wave group velocity dispersion curves and  
15 estimated their associated uncertainties based on seasonal variability. Group velocity  
16 maps calculated at periods of 8–23 s reveal a close correlation between Rayleigh wave  
17 group velocity and major geological features: in particular, the major sedimentary basins  
18 are clearly imaged at 8–18 s periods, and a number of previously reported boundaries  
19 between basement terranes in central New Zealand are also manifest at this periods. We  
20 have also constructed four 1-D shear velocity models to illustrate the vertical resolution  
21 obtainable with these measurements.  
22  
23

24  
25 At periods longer than approximately 20–25 s, in particular, it is clear that constraints  
26 imposed on the seismic network by New Zealand's long, narrow geometry impose  
27 limitations on surface wave analysis and the analysis of structure deeper than  
28 approximately 30 km. In order to image better New Zealand's deeper structure using  
29 these techniques, broadband ocean bottom seismometers (OBSs) deployed on the  
30 continental shelf appear necessary. OBS arrays deployed on either side of the country  
31 would improve both the number of paths along which long-period measurements can be  
32 made and the azimuthal distribution of those paths.  
33  
34

35  
36 This study is intended to serve as a foundation for several lines of future research. Among  
37 these are the use of horizontal-component seismograms (which would enable Love waves  
38 to be analyzed), measurement of phase velocity of both Rayleigh and Love waves, and  
39 cross-correlation amongst local network stations at frequencies perhaps as high as 1 Hz.  
40 Ongoing research will make use of longer-duration data sets and data acquired with new  
41 broadband seismometers installed in the far south of the South Island in early 2006 as  
42 part of GeoNet's ongoing expansion, augmented with data recorded during short-term  
43 deployments. This will improve the propagation path coverage and long-period SNR  
44 characteristics of the group velocity measurements, and enable us to perform 3-D  
45 anisotropic shear wave velocity tomography.  
46  
47  
48  
49  
50  
51  
52  
53  
54  
55  
56  
57  
58  
59  
60



## 7. Acknowledgments

The authors gratefully acknowledge the New Zealand GeoNet Project (<http://www.geonet.org.nz>) and the IRIS Data Management Center for access to the data on which this research is based. We particularly thank Mark Chadwick and Ken Gledhill, GNS Science, for help with obtaining GeoNet data and discussions regarding the SNR characteristics of different GeoNet instruments. We also thank Indrajit Das, Indian Institute of Technology at Kharagpur, for help in implementing the noise correlation algorithms at VUW during a short-term internship. This work was undertaken with support from the Foundation for Research, Science and Technology.

## 8. References

- Anderson, H.J., 1979. A geophysical study of the Westport, Inangahua and Murchison Basins, West Coast, South Island, *Geophysics Division, Department of Scientific and Industrial Research, Research Report*, **148**, 53 p.
- Ansell, J.H. and Bannister, S., 1996. Shallow morphology of the subducted Pacific plate along the Hikurangi margin, New Zealand, *Phys. Earth. Planet. In.*, **93**, 3–10.
- Baldock, G. and Stern, T., 2005. Width of mantle deformation across a continental transform: Evidence from upper mantle (Pn) seismic anisotropy measurements, *Geology*, **33**(9), 741–744.
- Barmin, M.P., Ritzwoller, M.H., and Levshin, A.L., 2001. A fast and reliable method for surface wave tomography, *Pure Appl. Geophys.*, **158**, 1351 - 1375.
- Beanland, S., Melhuish, A., Nicol, A., and Ravens, J., 1998. Structure and deformational history of the inner forearc region, Hikurangi subduction margin, New Zealand, *New Zeal. J. Geol. Geophys.*, **41**, 325–342.
- Bensen, G.D., Barmin, M.P., Levshin, A.L., Lin, F., Moschetti, M.P., Shapiro, N.M., Yang, Y. and Ritzwoller, M.H. 2006. Processing ambient noise seismic data to obtain reliable broadband surface wave dispersion measurements, manuscript in preparation, *Geophys. J. Int.*, submitted.
- Brisbourne, A.M., and Stuart, G.W. 1998. Shear-wave velocity structure beneath North Island, New Zealand, from Rayleigh-wave interstation phase velocities, *Geophys. J. Int.*, **133**, 175–184.
- Brisbourne, A., Stuart, G., and Kendall, J.-M. 1999. Anisotropic structure of the

- Hikurangi subduction zone, New Zealand - integrated interpretation of surface-wave and body-wave observations, *Geophys. J. Int.*, **137**, 214–230.
- Butler, R., et al. 2004. Global seismographic network surpasses its design goal, *Eos Trans. AGU*, **85**(23), 225.
- Cho, K.H., Hermann, R.B., Ammon, C.J. & Lee, K. 2006. Imaging the upper crust of the Korean Peninsula by surface-wave tomography, *Bull. Seism. Soc. Amer.*, submitted.
- Campillo, M. & Paul, A. 2003. Long-range correlations in the diffuse seismic coda, *Science*, **299**, 547–549.
- Dahlen, F.A. and Zhou, Y. 2006. Surface wave group delay and attenuation kernels, *Geophys. J. Int.*, in press.
- Davey, F. J., Henrys, S. A. & Lodolo, E. 1995. Asymmetric rifting in a continental back-arc environment, North Island, New Zealand. *J. Volcanol. Geoth. Res.*, **68**, 209–238.
- Davey, F.J., et al., 1998. Preliminary results from a geophysical study across a modern continent-continent collisional plate boundary — The Southern Alps, New Zealand, *Tectonophys.*, **288**, 221–235.
- Derode, A., Larose, E., Tanter, M., de Rosny, J., Tourim, A., Campillo, M. & Fink, M. 2003. Recovering the Green's function from field-field correlations in an open scattering medium (L), *J. Acoust. Soc. Am.*, **113**, 2973–2976.
- Eberhart-Phillips, D. & Bannister, S. 2002. Three-dimensional crustal structure in the Southern Alps region of New Zealand from inversion of local earthquake and active source data. *J. Geophys. Res.*, **107**, 2262.
- Eberhart-Phillips, D. & McVerry, G. 2003. Estimating slab earthquake response spectra from a 3D Q model. *Bull. Seismol. Soc. Am.*, **93**, 2649–2663.
- Godfrey, N.J., Davey, F.J., Stern, T.A. & Okaya, D. 2001. Crustal structure and thermal anomalies of the Dunedin region, South Island, New Zealand. *J. Geophys. Res.*, **106**, 30835–30848.
- Godfrey, N.J., Christensen, N.I. & Okaya, D.A. 2002. Anisotropy of schists: contribution of crustal anisotropy to active source seismic experiments and shear wave splitting observations. *J. Geophys. Res.*, **105**, 27991–28007.
- Gorman, R.M., Bryan, K. & Laing, A.K., 2003. Wave hindcast for the New Zealand



- 1  
2  
3  
4 region: nearshore validation and coastal wave climate. *New Zeal. J. Mar.*  
5 *Freshwat. Res.*, **37**, 567–588.  
6
- 7 Harrison, A.J. & White, R.S. 2004. Crustal structure of the Taupo Volcanic Zone, New  
8 Zealand: stretching and igneous intrusion. *Geophys. Res. Lett.*, **13**, L13615, 1–4.  
9
- 10 Henrys, S., Reyners, M., Pecher, I., Bannister, S., Nishimura, Y. & Maslen, G. 2006.  
11 Kinking of the subducting slab by escalator normal faulting beneath the North  
12 Island of New Zealand. *Geology*, **34**, 777–780.  
13
- 14 Horspool, N.A., Savage, M.K. & Bannister, S. 2006. Implications for intraplate  
15 volcanism and back-arc deformation in northwestern New Zealand, from joint  
16 inversion of receiver functions and surface waves. *Geophys. J. Int.*, **166**,  
17 1466–1483.  
18
- 19 King, P.R. & Thrasher, G.P. 1996. Cretaceous-Cenozoic geology and petroleum systems  
20 of the Taranaki Basin, New Zealand. Lower Hutt: Institute of Geological &  
21 Nuclear Sciences. *Institute of Geological & Nuclear Sciences monograph*, **13**,  
22 243 p.  
23
- 24 Laing, A.K. 2000. New Zealand wave climate from satellite observations, *New Zeal. J.*  
25 *Mar. Freshwat. Res.*, **34**, 745–749.  
26
- 27 Larose, E., Derode, A., Corenec, D., Margerin, L. & Campillo, M. 2005. Passive  
28 retrieval of Rayleigh waves in disordered elastic media, *Phys. Rev. E.*, **72**, 046607,  
29 doi:10.113/PhysRevE.72.046607.  
30
- 31 Levshin, A.L. & Ritzwoller, M.H., 2001. Automated detection, extraction, and  
32 measurement of regional surface waves, *Pure Appl. Geophys.*, **158**, 1531–1545.  
33
- 34 Levshin, A.L., Barmin, M.P., Ritzwoller, M.H. & Trampert, J. 2005. Minor-arc and  
35 major-arc global surface wave diffraction tomography, *Phys. Earth Planet. Int.*,  
36 **149**, 205–223.  
37
- 38 Lin, F., Ritzwoller, M.H. & Shapiro, N.M. 2006. Is ambient noise tomography across  
39 ocean basins possible? *Geophys. Res. Lett.*, **33**, L14304,  
40 doi:10.1029/2006GL026610.  
41
- 42 Mooney, H. 1970. Upper mantle inhomogeneity beneath New Zealand: Seismic evidence,  
43 *J. Geophys. Res.*, **75**, 285–309.  
44
- 45 Mortimer, N. 1993. Metamorphic zones, terranes and Cenozoic faults in the Marlborough  
46 Schist, New Zealand, *New Zeal. J. Geol. Geophys.*, **36**, 357–368.  
47  
48  
49  
50  
51  
52  
53  
54  
55  
56  
57  
58  
59  
60

- 1  
2  
3  
4 Mortimer, N., Tulloch, A.J. & Ireland, T.R. 1997. Basement geology of Taranaki and  
5 Wanganui Basins, New Zealand, *New Zeal. J. Geol. Geophys.*, **40**, 223–236  
6  
7 Mortimer, N. 2004 New Zealand's geological foundations, *Gondwana Research*, **7**(1),  
8 261–272  
9  
10 Moschetti, M.P., Ritzwoller, M.H. & Shapiro, N.M. 2005. California surface wave  
11 tomography from ambient seismic noise: Tracking the progress of the USArray  
12 Transportable Network, *Eos Trans. AGU*, **86**(52), Fall Meet. Suppl., Abstract  
13 S31A-0276.  
14  
15  
16  
17 Okaya, D., Henrys, S. & Stern, T. 2002. Double-sided onshore-offshore seismic imaging  
18 of a plate boundary: "super-gathers" across South Island, New Zealand,  
19 *Tectonophys.*, **355**, 247–263.  
20  
21  
22 Paul, A., Campillo, M., Margerin, L., Larose, E. & Derode, A. 2005. Empirical synthesis  
23 of time-asymmetrical Green functions from the correlation of coda waves, *J.*  
24 *Geophys. Res.*, **110**, B08302, doi:10.1029/2004JB003521.  
25  
26  
27 Pickrill, R.A. & Mitchell, J.S. 1979. Ocean wave characteristics around New Zealand.  
28 *New Zeal. J. Mar. Fresh. Res.*, **13**, 501–520.  
29  
30  
31 Reyners, M., et al. 2006. Imaging subduction from the trench to 300 km depth beneath  
32 the central North Island, New Zealand, with Vp and Vp/Vs, *Geophys. J. Int.*,  
33 **165**(2), 565–583.  
34  
35  
36 Ritzwoller, M.H. & Levshin, A.L. 1998. Eurasian surface wave tomography: group  
37 velocities, *J. Geophys. Res.*, **103**, 4839–4878.  
38  
39 Ritzwoller, M.H., Shapiro, N.M., Barmin, M.P., & Levshin, A.L. 2002. Global surface  
40 wave diffraction tomography, *J. Geophys. Res.*, **107**, B12,  
41 10.1029/2002JB001777.  
42  
43  
44 Roux, P., Sabra, K.G., Gerstoft, P., Kuperman, W.A. & Fehler, M.C. 2005. P-waves from  
45 cross-correlation of seismic noise, *Geophys. Res. Lett.*, **32**, L19393,  
46 doi:10.1029/2005GL023803.  
47  
48  
49 Sabra, K.G., Gerstoft, P., Roux, P., Kuperman, W.A. & Fehler, M.C. 2005a. Extracting  
50 time-domain Green's function estimates from ambient seismic noise, *Geophys.*  
51 *Res. Lett.*, **32**, L03310, doi:10.1029/2004GL021862.  
52  
53  
54 Sabra, K.G., Gerstoft, P., Roux, P., Kuperman, W.A. & Fehler, M.C. 2005b. Surface  
55 wave tomography from microseism in southern California, *Geophys. Res. Lett.*,  
56 **32**, L14311, doi:10.1029/2005GL023155.  
57  
58  
59  
60

- 1  
2  
3  
4 Salmon, M., Bannister, S., Bibby, H., Savage, M.K. & Stern T.A. 2003. Attenuation and  
5 electrical resistivity in an asymmetric back arc extensional environment. *Eos*  
6 *Trans. AGU*, 84(46), Fall Meet. Suppl., Abstract S22B-0450.
- 7  
8  
9 Savage, M.K., Fisher, K.M. & Hall, C.E. 2004. Strain modelling, seismic anisotropy, and  
10 coupling at strike-slip boundaries: applications in New Zealand and the San  
11 Andreas fault, in *Vertical coupling and decoupling in the lithosphere*, J. Grocott,  
12 et al., Editors, Geological Society, London, p 9–40.
- 13  
14  
15 Scherwath, M., et al. 2002. Pn anisotropy and distributed upper mantle deformation  
16 associated with a continental transform fault, *Geophys. Res. Lett.*, **29**(8), 16–1.
- 17  
18  
19 Scherwath, M., Stern., D., Davey, F., Davies, R., Kleffmann, S. & Okaya, D. 2003.  
20 Lithospheric structure across oblique continental collision in New Zealand from  
21 wide-angle P-wave modelling, *J. Geophys. Res.*, **108**, 2566,  
22 doi:10.1029/2004GL019491.
- 23  
24  
25 Shapiro, N.M. & Campillo, M. 2004. Emergence of broadband Rayleigh waves from  
26 correlations of the ambient seismic noise, *Geophys. Res. Lett.*, **31**, L07614,  
27 doi:10.1029/2004GL019491.
- 28  
29  
30 Shapiro, N.M. & Ritzwoller, M.H., 2002. Monte-Carlo inversion for a global shear  
31 velocity model of the crust and upper mantle, *Geophys. J. Int.*, **151**, 88–105.
- 32  
33  
34 Shapiro, N.M., Campillo, M., Stehly, L. & Ritzwoller, M.H. 2005. High resolution  
35 surface wave tomography from ambient seismic noise, *Science*, **307**, 1615–1618.
- 36  
37  
38 Sherburn, S., White, R.S. & Chadwick, M. 2006. Three-dimensional tomographic  
39 imaging of the Taranaki volcanoes, New Zealand. *Geophys. J. Int.*, **166**, 957–969.
- 40  
41  
42 Sieminski, A., Leveque, J.-J. & Debayle, E. 2004. Can finite-frequency effects be  
43 accounted for in ray theory surface wave tomography? *Geophys. Res. Lett.*, **31**,  
44 L24614, doi:10.1029/2004GL021402.
- 45  
46  
47 Snieder, R. 2004. Extracting the Green's function from the correlation of coda waves: A  
48 derivation based on stationary phase, *Phys. rev. E*, **69**, 046610.
- 49  
50  
51 Spetzler, J., Trampert, J. & Snieder, R., 2002. The effects of scattering in surface wave  
52 tomography, *Geophys. J. Int.*, **149**, 755–767.
- 53  
54  
55 Stern, T.A. 1987. Asymmetric back-arc spreading, heat flux and structure associated with  
56 the Central Volcanic Region of New Zealand. *Earth and Planetary Sci. Lett.*, **85**,  
57 265–276.
- 58  
59  
60

- 1  
2  
3  
4 Stern, T., et al., 2000. Teleseismic P wave delays and modes of shortening the mantle  
5 lithosphere beneath South Island, New Zealand, *J. Geophys. Res.*, **105**,  
6 21615–21631.  
7
- 8  
9 Stern, T., 2006. Subduction at a continental margin: kinematics and dynamics of the  
10 central North Island, New Zealand, *Revs. Geophys.*, in press.  
11
- 12  
13 Stratford, W.R. & Stern, T.A. 2006. Crust and mantle structure of continental backarc:  
14 central North Island, New Zealand, *Geophysical J. Int.*, **166**, 469–484, doi:  
15 10.1111/j.1365-246X.2006.02967.x.  
16
- 17  
18 Uruski, C.I., Cook, R.A., Herzer, R.H. & Isaac, M.J. 2004. Petroleum geology of the  
19 Northland sector of the greater Taranaki Basin, 10 p. In: 2004 *New Zealand*  
20 *Petroleum Conference proceedings*. Wellington: Crown Minerals, Ministry of  
21 Economic Development.  
22
- 23  
24 Wapenaar, K. 2004. Retrieving the elastodynamic Green's function of an arbitrary  
25 inhomogeneous medium by cross correlation, *Phys. Rev. Lett.*, **93**, 254301,  
26 doi:10.1103/PhysRevLett.93.254301.  
27
- 28  
29 Weaver, R.L. & Lobkis, O.I. 2001a. Ultrasonics without a source: Thermal fluctuation  
30 correlation at MHz frequencies, *Phys. Rev. Lett.*, **87**, 134301.  
31
- 32  
33 Weaver, R.L. & Lobkis, O.I. 2001b. On the emergence of the Green's function in the  
34 correlations of a diffuse field, *J. Acoust. Soc. Am.*, **110**, 3011–3017.  
35
- 36  
37 Weaver, R.L. & Lobkis, O.I. 2004. Diffuse fields in open systems and the emergence of  
38 the Green's function, *J. Acoust. Soc. Am.*, **116**, 2731–2734.  
39
- 40  
41 Wood, R. & Woodward, D. 2002. Sediment thickness and crustal structure of offshore  
42 western New Zealand from 3D gravity modelling. *New Zeal. J. Geol. Geophys.*,  
43 **45**, 243–255.  
44
- 45  
46 Yang, Y., Ritzwoller, M.H., Levshin, A.L. & Shapiro, N.M. 2006. Ambient noise  
47 Rayleigh wave tomography across Europe, *Geophys. J. Int.*, in press.  
48
- 49  
50 Yao, H., van der Hilst, R.D. & de Hoop, M.V. 2006. Surface-wave tomography in SE  
51 Tibet from ambient seismic noise and two-station analysis: I. — Phase velocity  
52 maps, *Geophys. J. Int.*, **166**, 732–744.  
53
- 54  
55 Yoshizawa, K. & Kennett, B.L.H. 2002. Determination of the influence zone for surface  
56 wave paths, *Geophys. J. Int.*, **149**, 440–453.  
57
- 58  
59 Zhou, Y., Dahlen, F.A. & Nolet, G. 2004. 3-D sensitivity kernels for surface-wave  
60

observables, *Geophys. J. Int.*, **158**, 142–168.

## 9. Figure Captions

**Figure 1.** The seismic stations used in this study: 41 stations from the New Zealand GeoNet Project and one (SNZO) from the Global Seismic Network (Butler et al., 2004).

**Figure 2.** A broadband (5–100 s period) record section centred at station BFZ (Birch Farm, eastern Wairarapa, New Zealand). Both positive (“causal”) and negative (“acausal”) lags are shown. The gray lines mark “move-out” at velocities of  $2 \text{ km s}^{-1}$  and  $3 \text{ km s}^{-1}$ .

**Figure 3.** One-year stack of the symmetric-component cross-correlation signal observed for the station-pair DSZ–HIZ (Denniston North and Hauti) filtered into various period bands.

**Figure 4.** (a) One-year cross-correlation between stations EAZ (Earnsclough) and THZ (Top House) showing the window defining the signal location outlined in red. The cross-correlation is the top waveform and the symmetric-component waveform is shown below it. (b) The spectrum of the signal-to-noise ratio of the positive (red) and negative (green) lags of the cross-correlation and the symmetric-component (black) shown in (a). (c) Frequency-time image of the symmetric-component shown in (a) and the measured raw group-speed curve, where warm colours indicate larger amplitudes. (d) Frequency-time image after phase-matched filtering based on the raw dispersion measurement. The black line is the raw dispersion measurement from (c), the magenta line is the group speed measurement from phase-matched filtering, and the vertical blue line is the cut-off period below which waves travelled more than 3 wavelengths between the two stations.

**Figure 5.** (a) Inter-station paths for the group speed measurements shown in (b). Paths through: an offshore basin (OUZ–QRZ; Omahuta and Quartz Range), the Southern Alps (DCZ–LTZ; Deep Cove and Lake Taylor Station), the eastern side of the South Island (KHZ–ODZ; Kahutara and Otahua Downs), and the North island (PXZ–WCZ; Pawanui and Waipu Caves). The colour codes in (a) and (b) are the same. Four locations, Hamilton, Taupo, Canterbury Basin, and Southern Alps, where we invert for 1D models in Section 5.2 are marked as stars here.

**Figure 6.** The measured group speed curves for twelve three-month stacks are shown by red lines and the curve for the one-year stack is shown with a black curve for stations THZ (Top House) and TUZ (Tuapeka). The variation between the separate three-month

stacks is used to estimate measurement uncertainties at each period.

**Figure 7.** The average standard deviation of group speed for each period band. For periods lying within two measurement bands, the band with the lowest average standard deviation is chosen to provide the group velocity measurement. The variation above 30 s period is mainly caused by the paucity of measurements.

**Figure 8.** (a) The total number of group speed measurements at each period after completion of data selection. (b) The average of the SNR across all acceptable measurements for each period. (c) The average of the standard deviation (STD) of the group speed measurements among the three-month stacks for each period, which is interpreted as the average measurement uncertainty. (d) As with (c), but for arrival times. Again, the variation above 30 s period mainly reflects the small number of measurements.

**Figure 9.** The inter-station paths for all the group speed measurements meeting the selection criteria at periods of 8 s, 13 s, 18 s, and 23 s. The circle in each map has radius equal to 3 wave lengths. Hence, for a station at the centre of the circle, the enclosed area is the region too close to pass the first selection criterion.

**Figure 10.** Estimated resolution at periods of 8 s, 13 s, 18 s, and 23 s. Resolution is defined as the standard deviation of the Gaussian fit to the resolution map at each model node (defined in km).

**Figure 11.** The estimated group velocity maps at periods of 8 s, 13 s, 18 s, and 23 s.

**Figure 12.** Histograms of travel time misfit after tomography at periods of 8 s, 13 s, 18 s, and 23 s. The standard deviation (std) of the misfit is also shown.

**Figure 13.** Interpretation of the group velocity maps. Refer to text for the abbreviations.

**Figure 14.** (a) The group velocity measurements at four positions (Taupo green, Hamilton blue, Canterbury Basin black, Southern Alps red). At each position four measurements are taken from the tomography maps. The smooth lines represent the best fitting dispersion curves from the 1D model in (b). The colour codes in (a) and (b) are the same.

**Figure 15.** Summary of ambient noise directionality at periods of 8 s, 13 s, 18 s, and 23 s. For each station pair separated by more than 1.5 wavelengths two arrows with opposite directions are plotted at each station. The length of each arrow is proportional to the SNR at positive or negative lag (whichever is appropriate) multiplied by the square root of the inter-station distance. The directions of the arrows point along the great-circle linking the

1  
2  
3  
4 stations. Three stations TOZ, KNZ, and WHZ with high local noise are also shown on the  
5 maps.  
6  
7  
8  
9  
10  
11  
12  
13  
14  
15  
16  
17  
18  
19  
20  
21  
22  
23  
24  
25  
26  
27  
28  
29  
30  
31  
32  
33  
34  
35  
36  
37  
38  
39  
40  
41  
42  
43  
44  
45  
46  
47  
48  
49  
50  
51  
52  
53  
54  
55  
56  
57  
58  
59  
60

For Peer Review

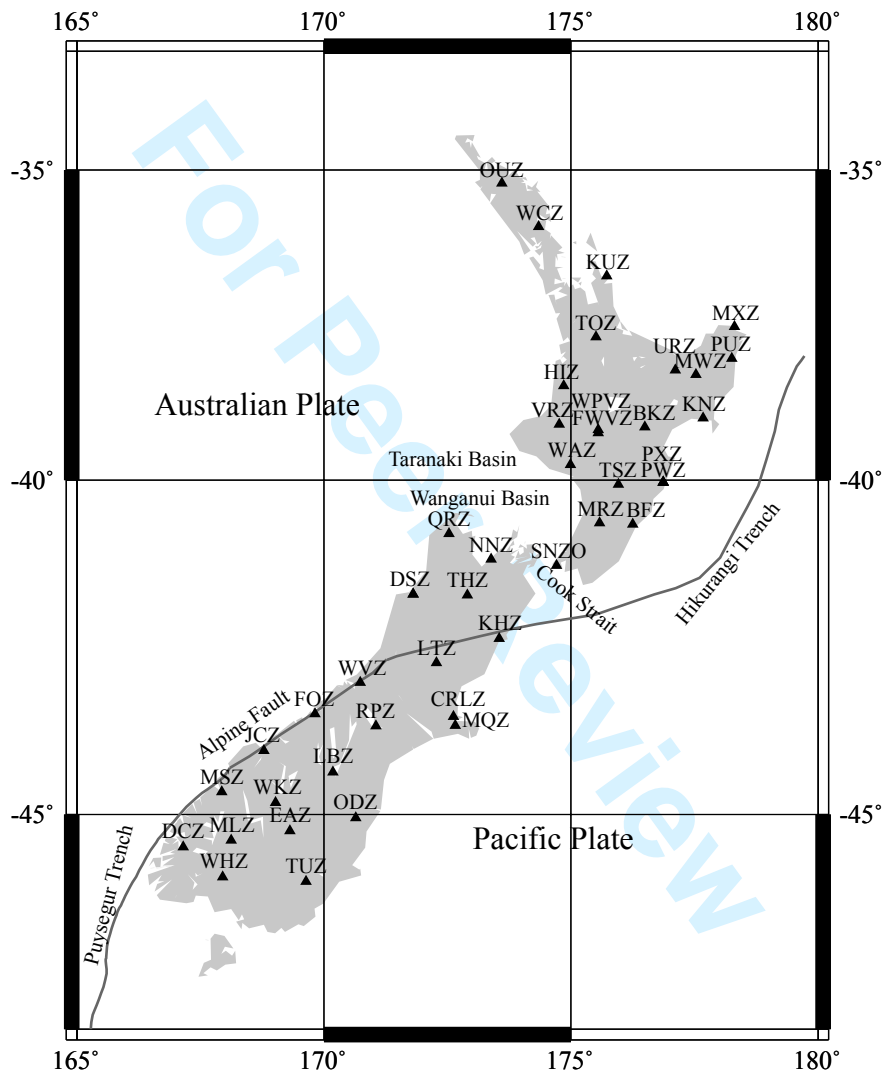


Fig. 1



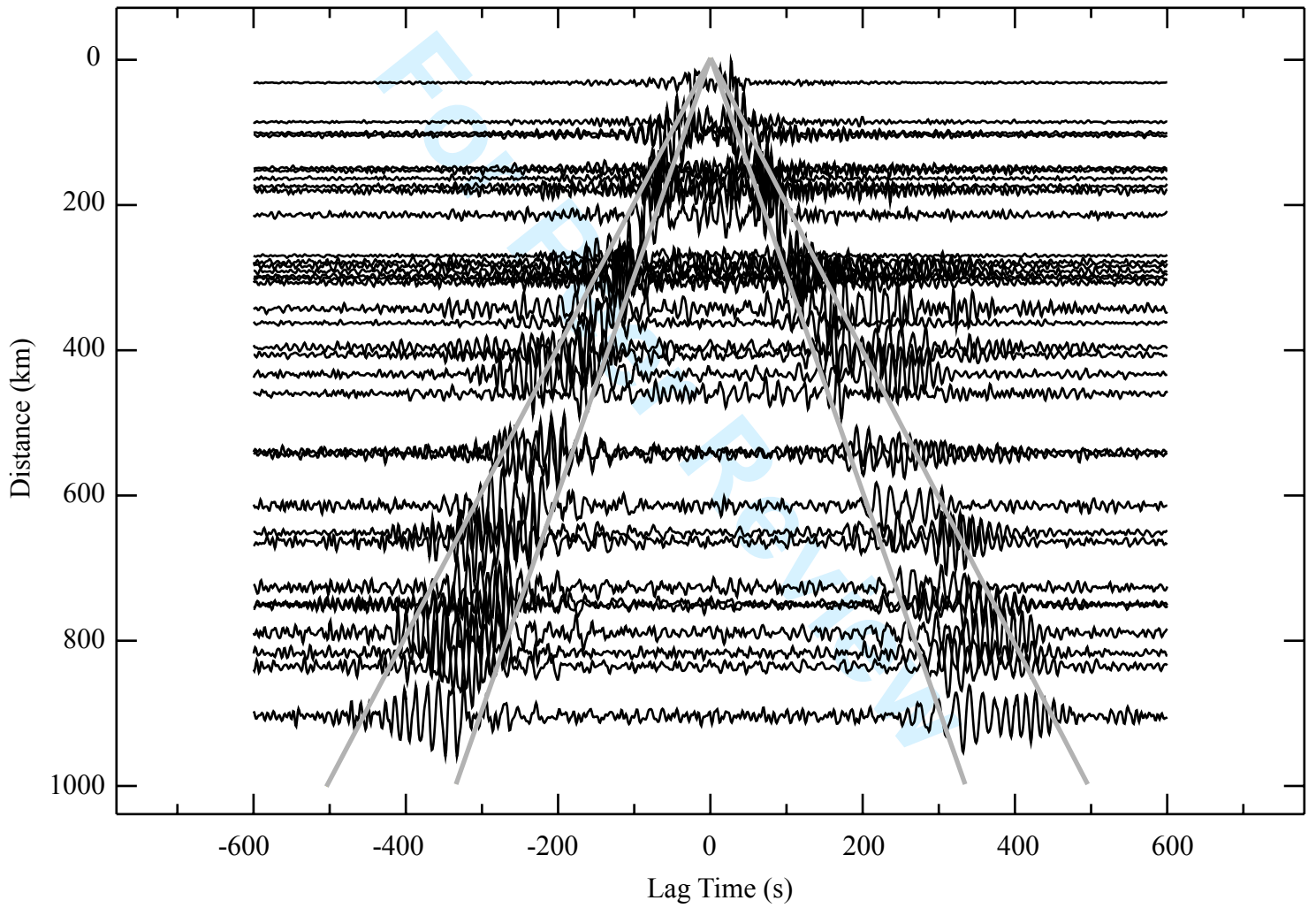


Fig. 2

1  
2  
3  
4  
5  
6  
7  
8  
9  
10  
11  
12  
13  
14  
15  
16  
17  
18  
19  
20  
21  
22  
23  
24  
25  
26  
27  
28  
29  
30  
31  
32  
33  
34  
35  
36  
37  
38  
39  
40  
41  
42  
43  
44  
45  
46  
47  
48  
49  
50  
51  
52  
53  
54  
55  
56  
57  
58  
59  
60

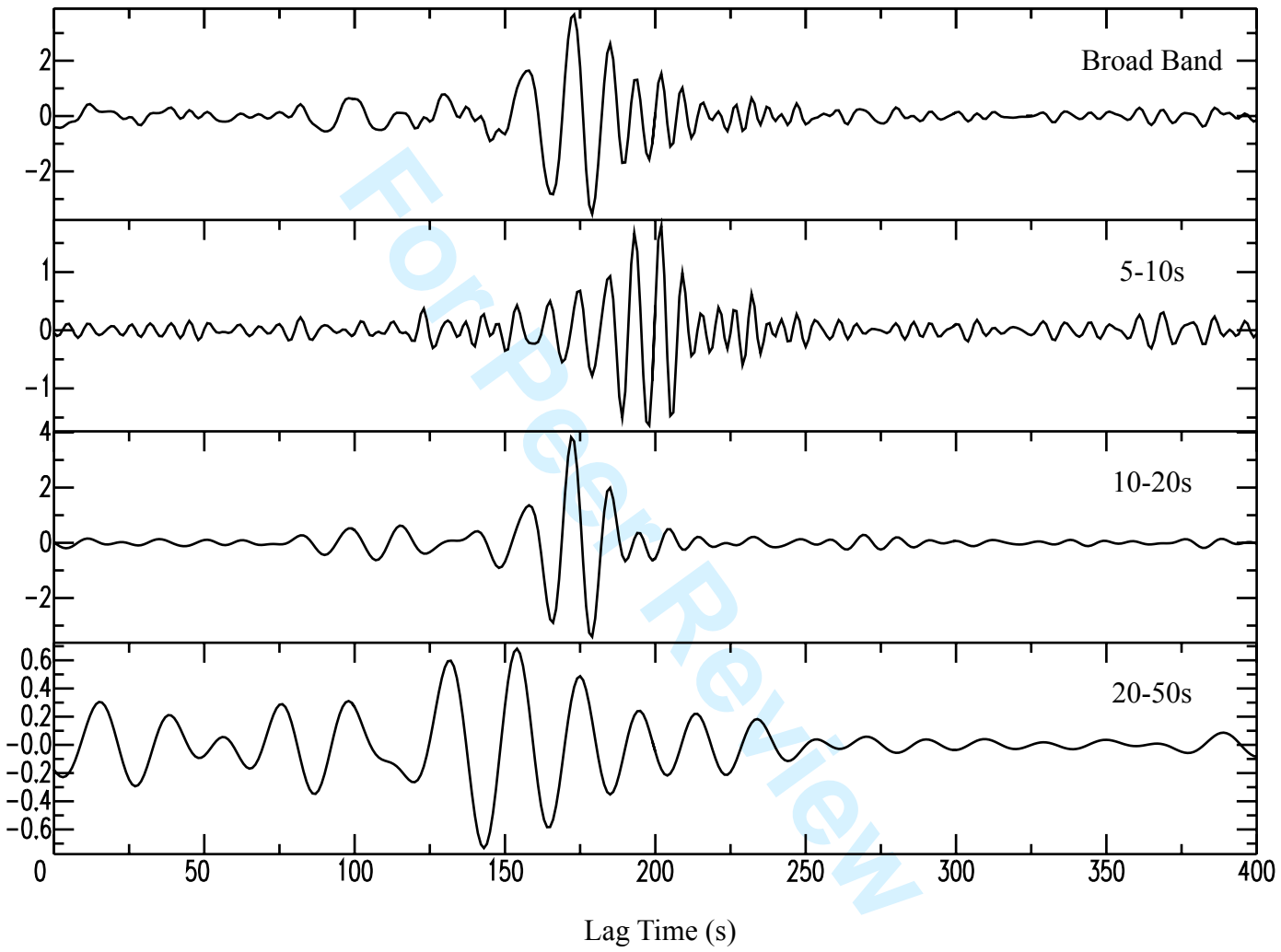


Fig.3

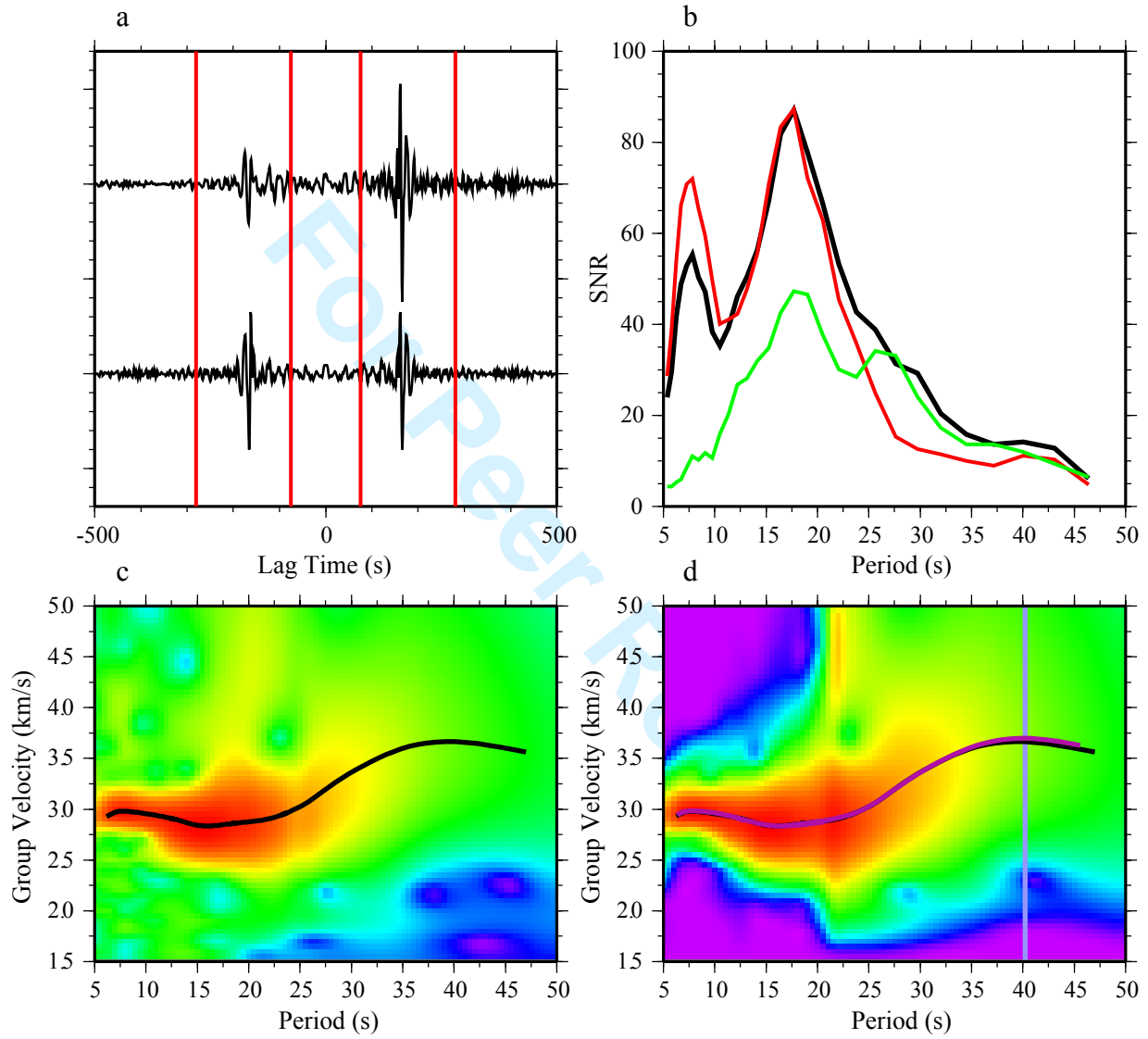


Fig. 4

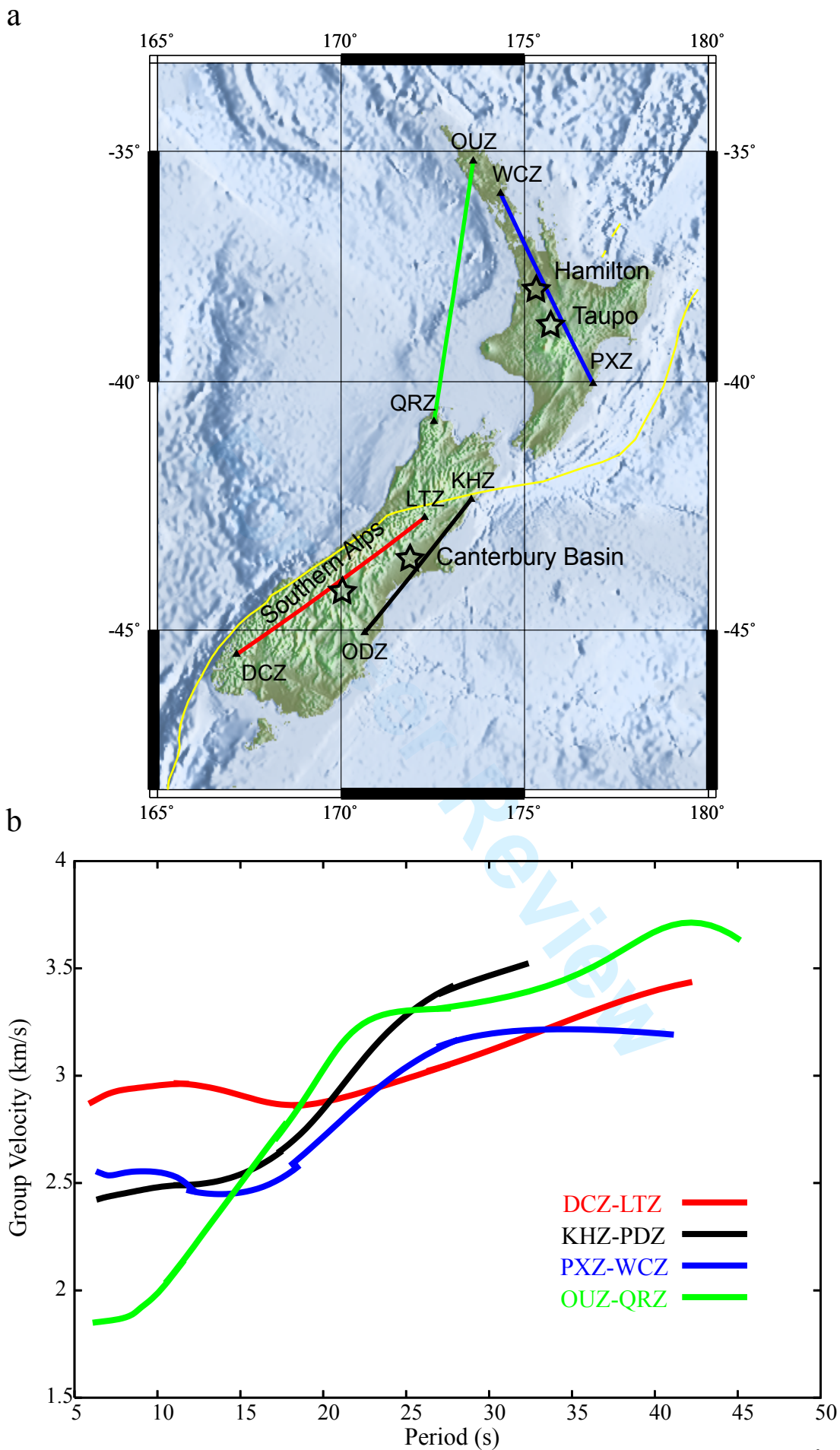


Fig. 5

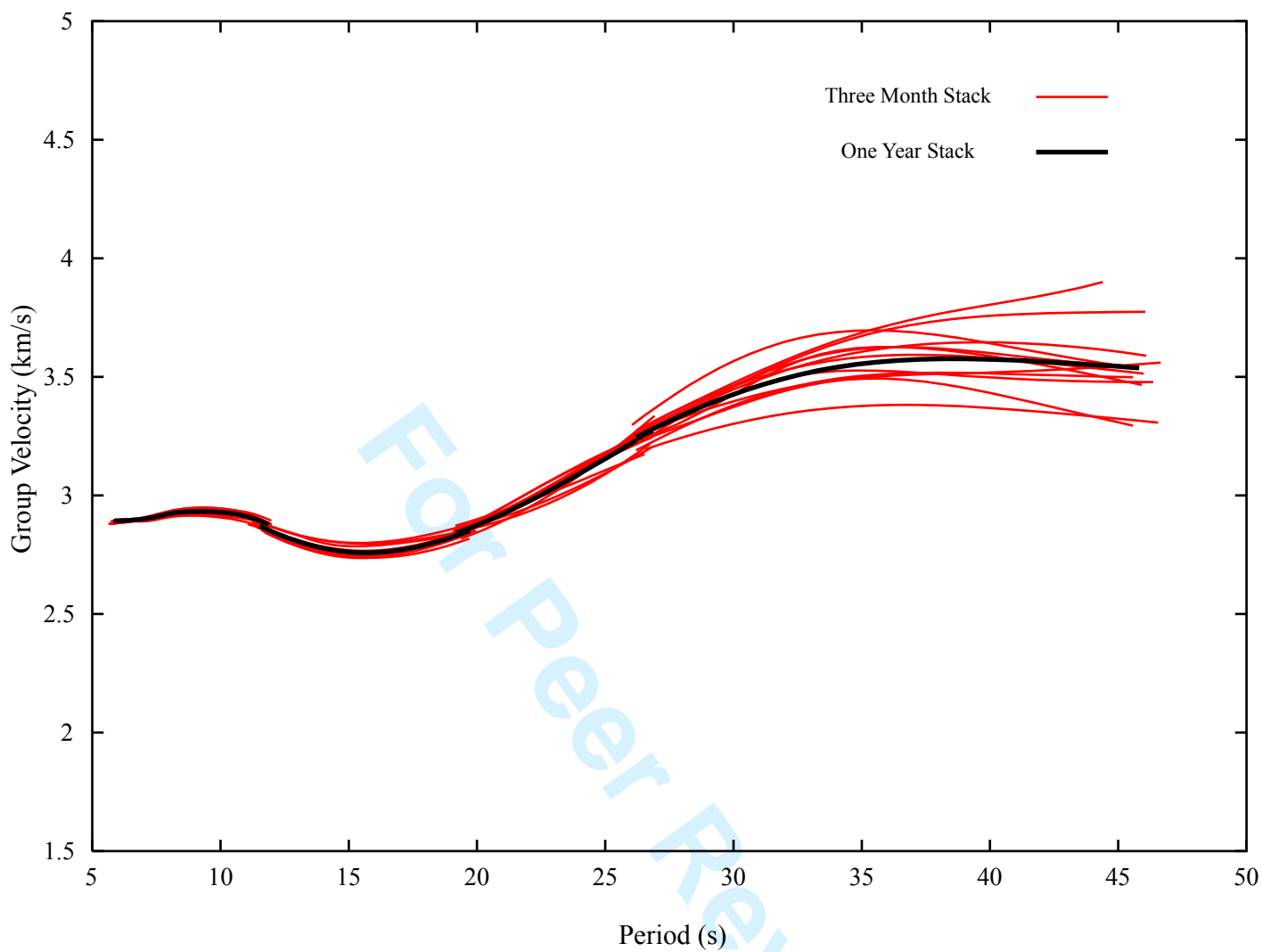


Fig. 6

1  
2  
3  
4  
5  
6  
7  
8  
9  
10  
11  
12  
13  
14  
15  
16  
17  
18  
19  
20  
21  
22  
23  
24  
25  
26  
27  
28  
29  
30  
31  
32  
33  
34  
35  
36  
37  
38  
39  
40  
41  
42  
43  
44  
45  
46  
47  
48  
49  
50  
51  
52  
53  
54  
55  
56  
57  
58  
59  
60

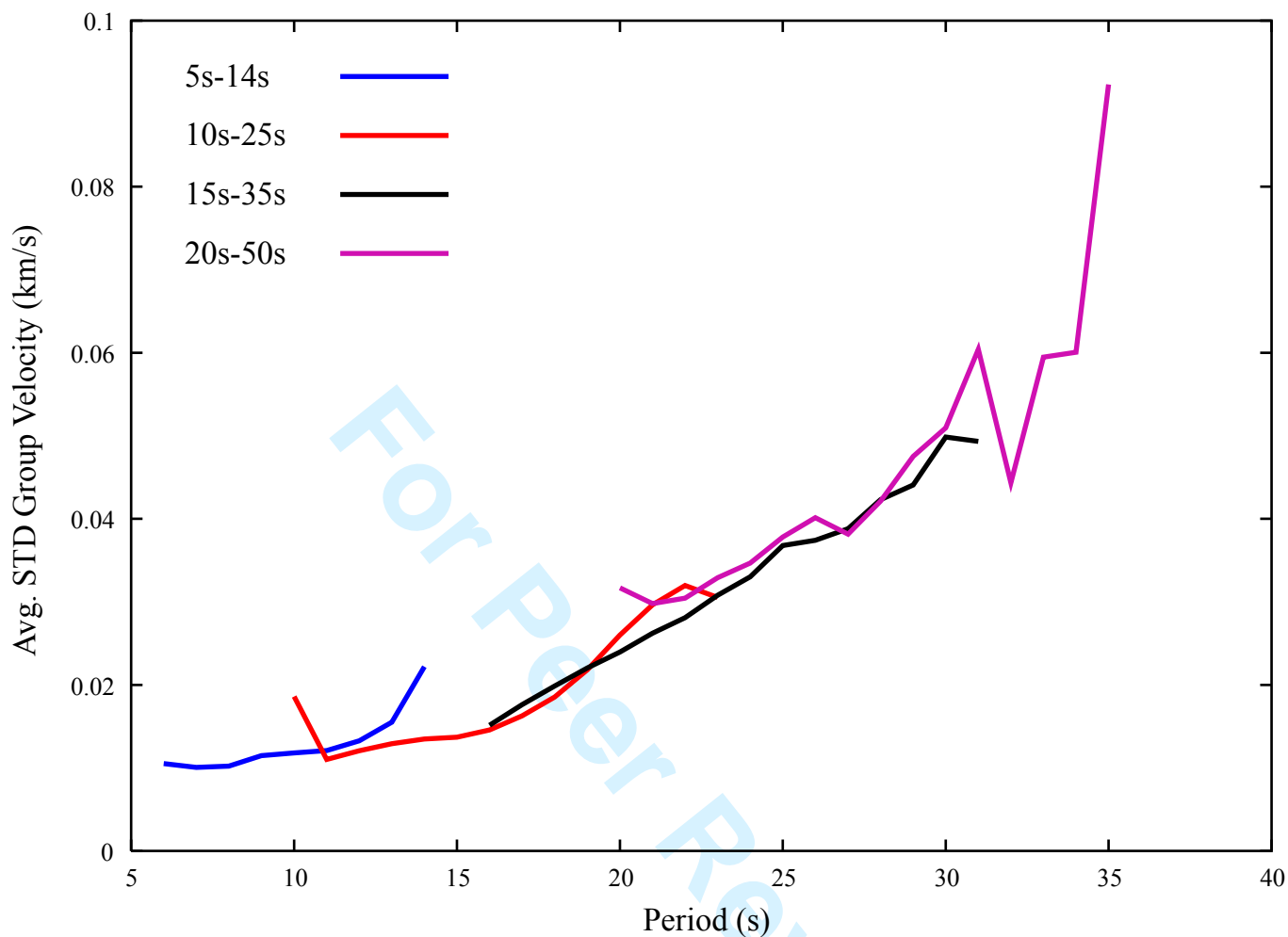


Fig. 7

1  
2  
3  
4  
5  
6  
7  
8  
9  
10  
11  
12  
13  
14  
15  
16  
17  
18  
19  
20  
21  
22  
23  
24  
25  
26  
27  
28  
29  
30  
31  
32  
33  
34  
35  
36  
37  
38  
39  
40  
41  
42  
43  
44  
45  
46  
47  
48  
49  
50  
51  
52  
53  
54  
55  
56  
57  
58  
59  
60

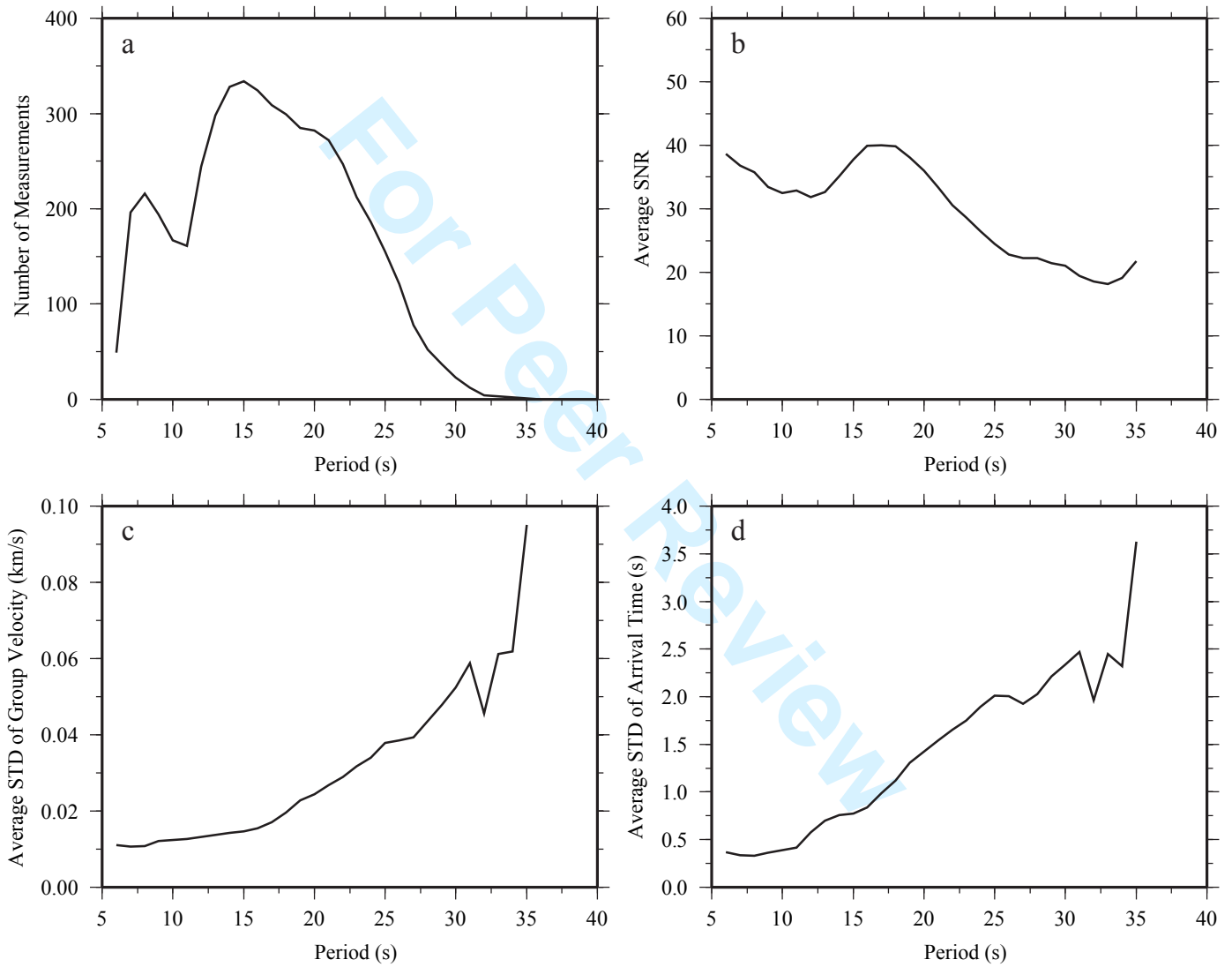


Fig.8

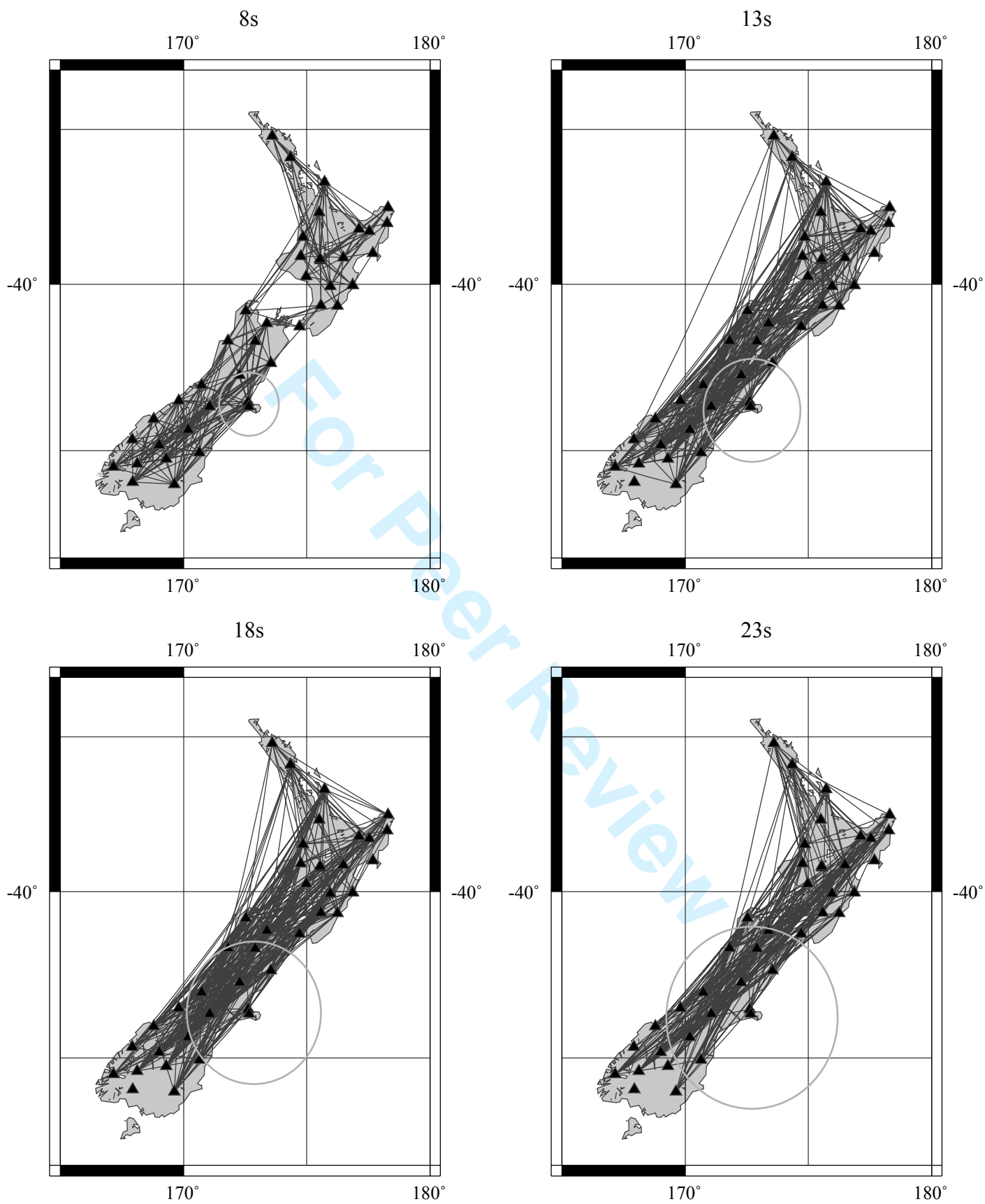


Fig. 9

1  
2  
3  
4  
5  
6  
7  
8  
9  
10  
11  
12  
13  
14  
15  
16  
17  
18  
19  
20  
21  
22  
23  
24  
25  
26  
27  
28  
29  
30  
31  
32  
33  
34  
35  
36  
37  
38  
39  
40  
41  
42  
43  
44  
45  
46  
47  
48  
49  
50  
51  
52  
53  
54  
55  
56  
57  
58  
59  
60



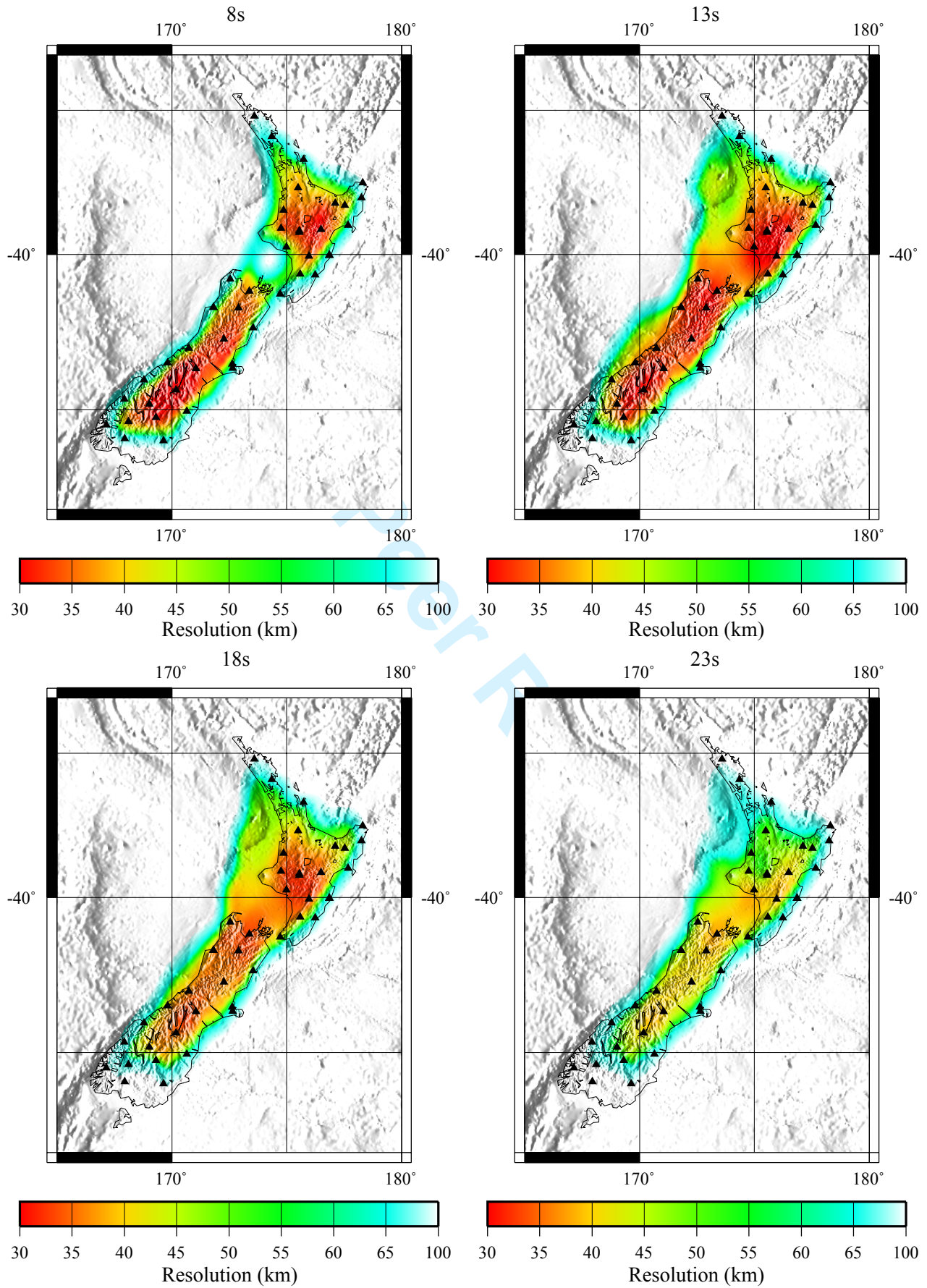


Fig.10

1  
2  
3  
4  
5  
6  
7  
8  
9  
10  
11  
12  
13  
14  
15  
16  
17  
18  
19  
20  
21  
22  
23  
24  
25  
26  
27  
28  
29  
30  
31  
32  
33  
34  
35  
36  
37  
38  
39  
40  
41  
42  
43  
44  
45  
46  
47  
48  
49  
50  
51  
52  
53  
54  
55  
56  
57  
58  
59  
60

1  
2  
3  
4  
5  
6  
7  
8  
9  
10  
11  
12  
13  
14  
15  
16  
17  
18  
19  
20  
21  
22  
23  
24  
25  
26  
27  
28  
29  
30  
31  
32  
33  
34  
35  
36  
37  
38  
39  
40  
41  
42  
43  
44  
45  
46  
47  
48  
49  
50  
51  
52  
53  
54  
55  
56  
57  
58  
59  
60

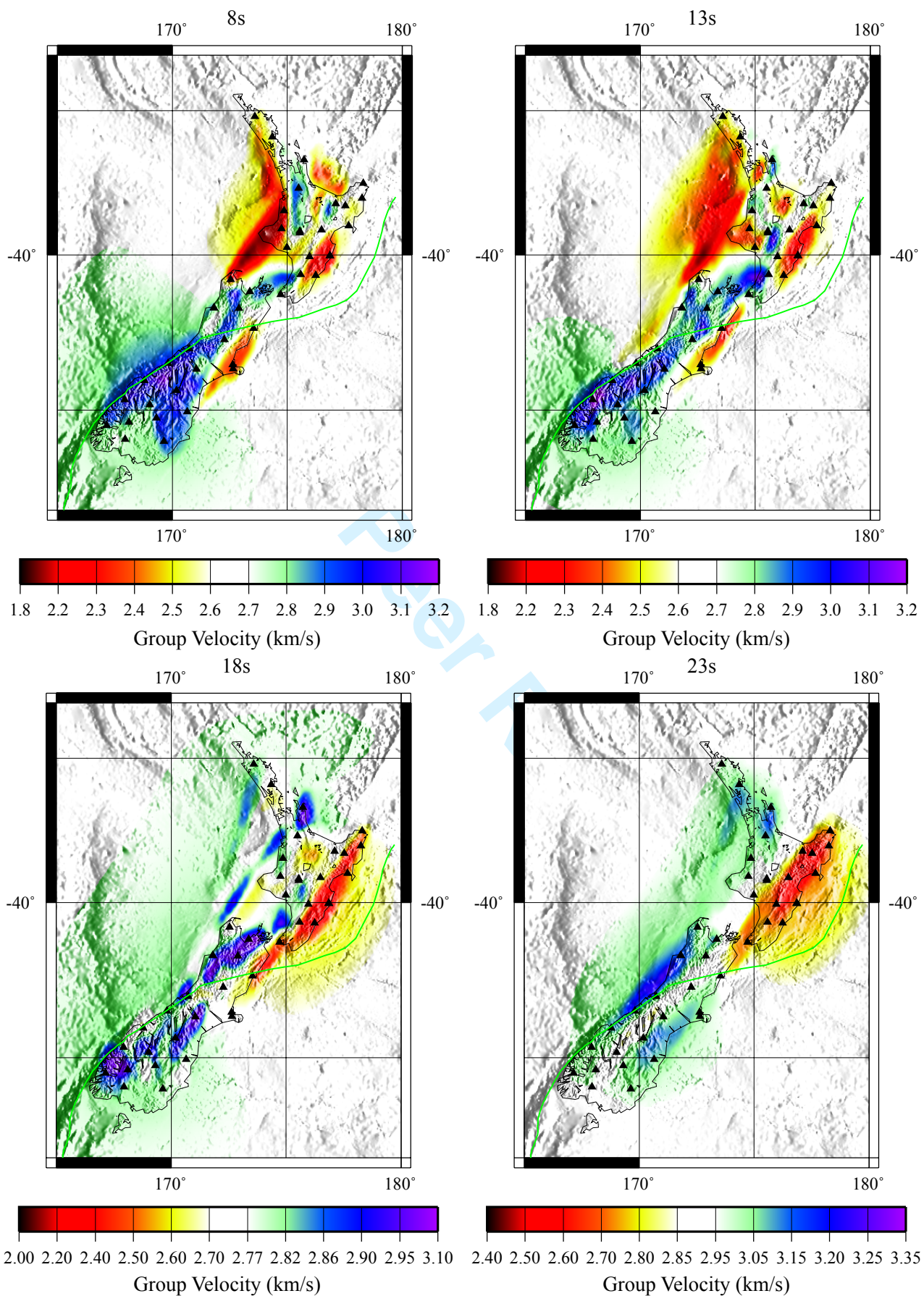


Fig. 11

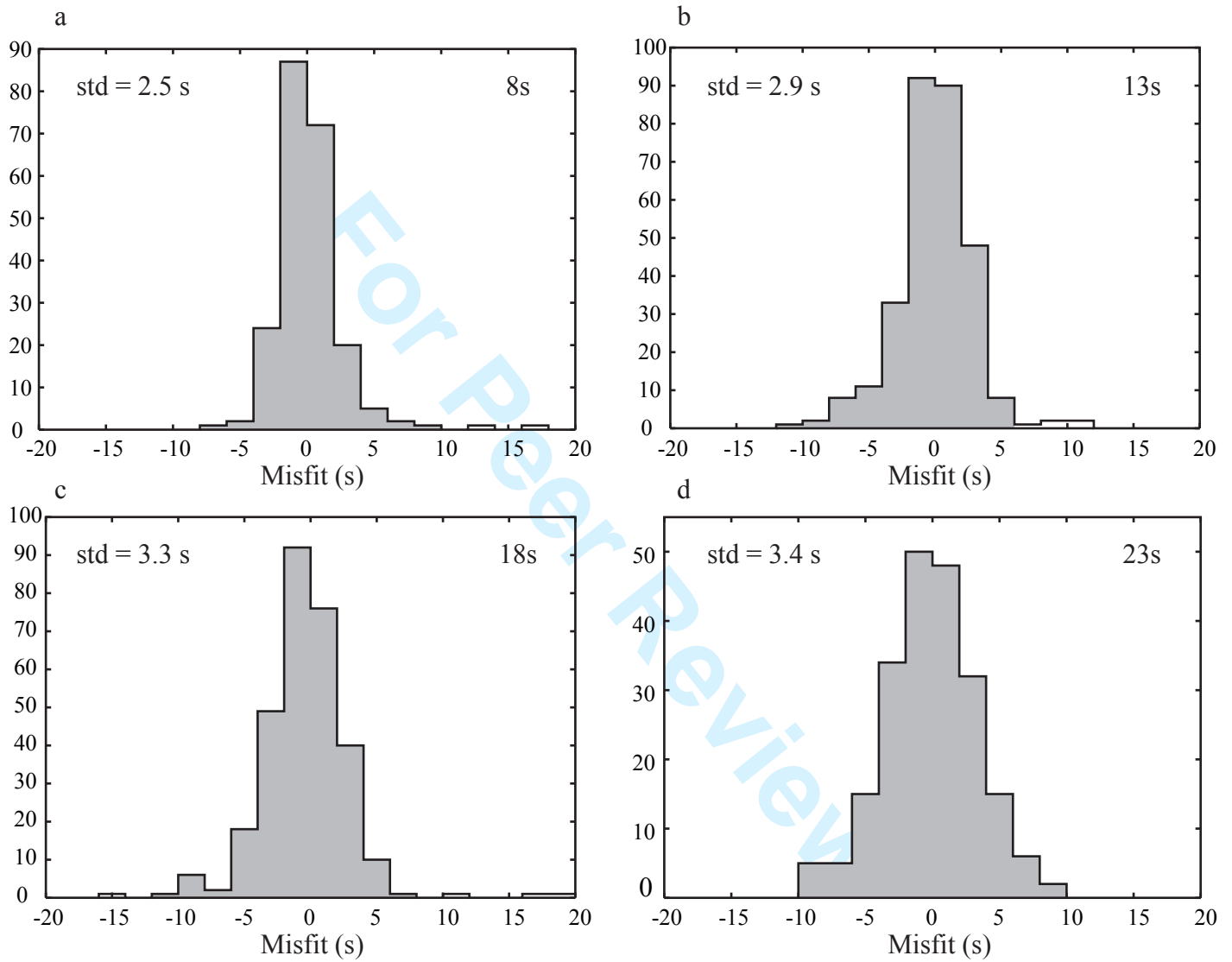


Fig. 12



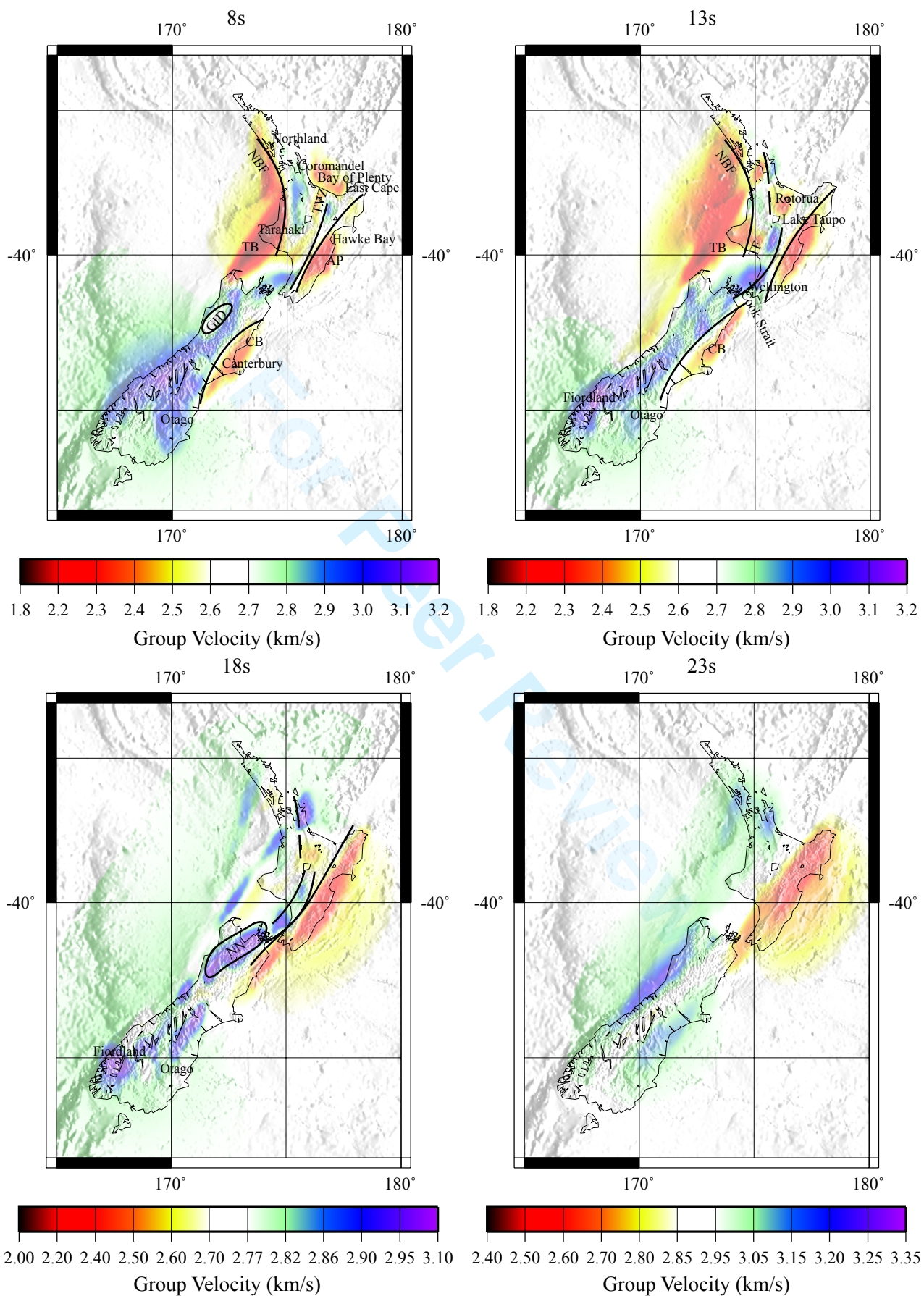


Fig. 13

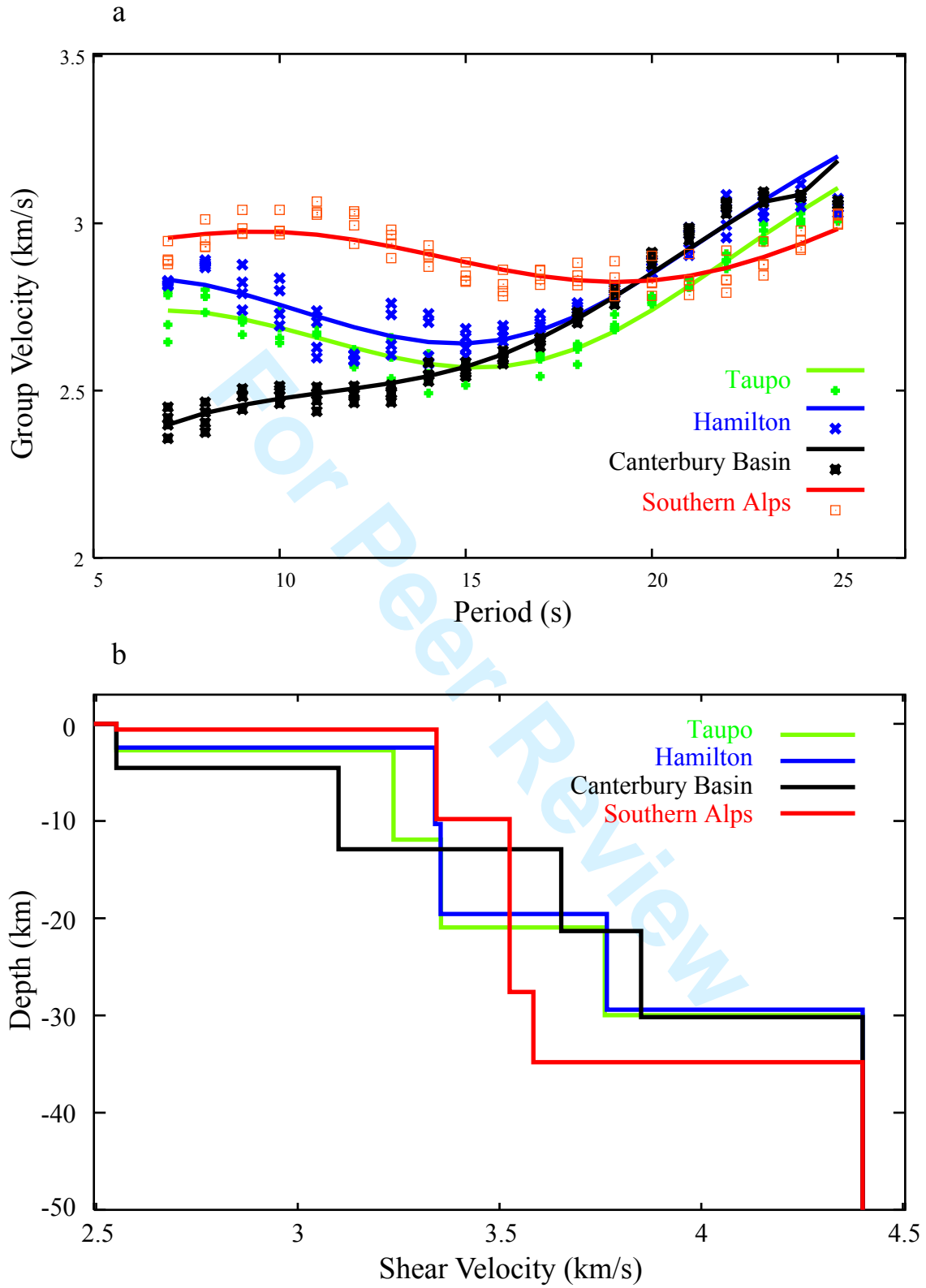


Fig. 14

1  
2  
3  
4  
5  
6  
7  
8  
9  
10  
11  
12  
13  
14  
15  
16  
17  
18  
19  
20  
21  
22  
23  
24  
25  
26  
27  
28  
29  
30  
31  
32  
33  
34  
35  
36  
37  
38  
39  
40  
41  
42  
43  
44  
45  
46  
47  
48  
49  
50  
51  
52  
53  
54  
55  
56  
57  
58  
59  
60

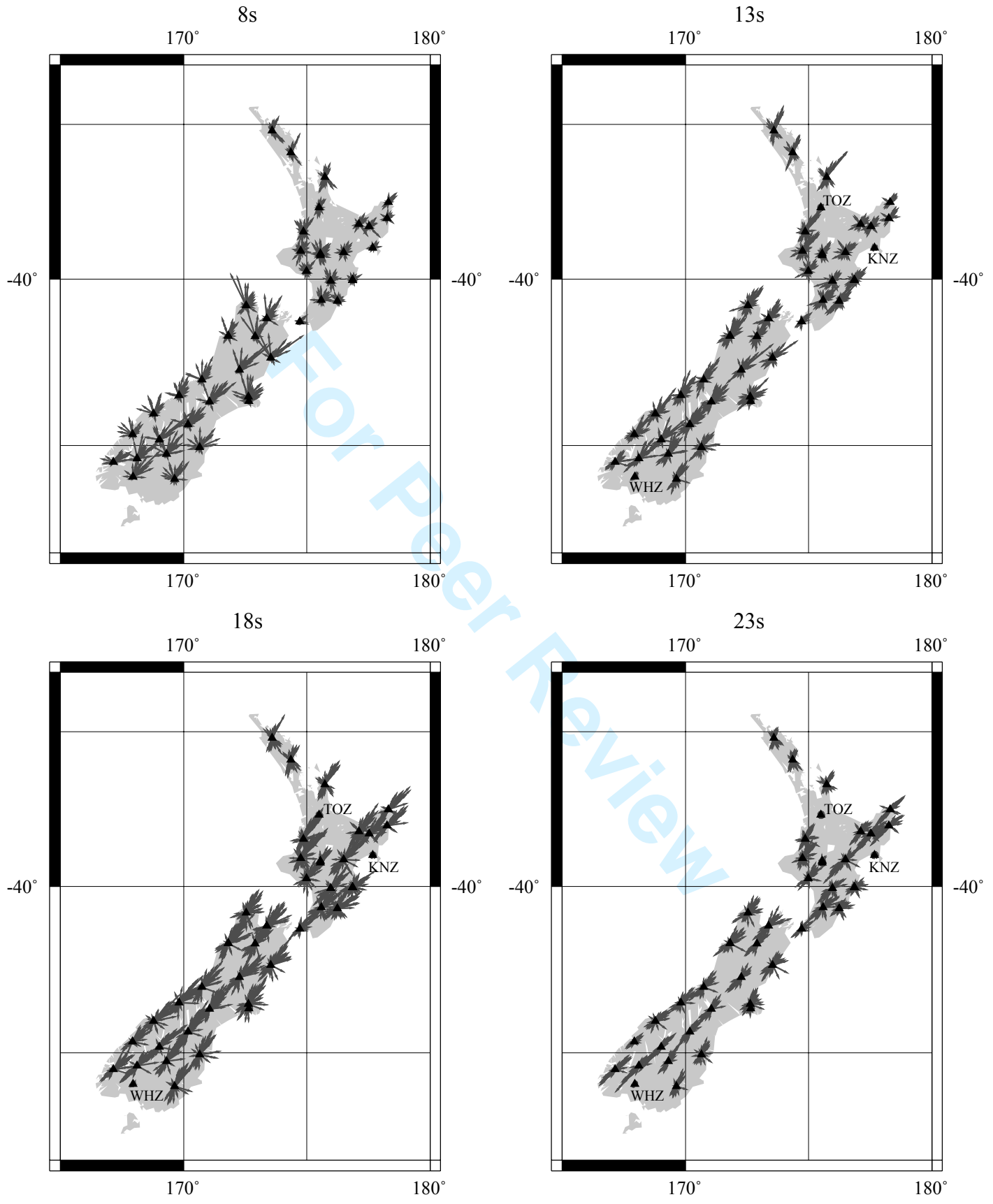


Fig. 15